catalysts

MDPI

Article

Structure–Activity Relationship Study of Mn/Fe Ratio Effects on Mn−Fe−Ce−O_x/γ-Al_2O_3 Nanocatalyst for NO Oxidation and Fast SCR Reaction

Yan Gao [1,2,3,*], Tao Luan [4], Mingyang Zhang [1,2,3], Wenke Zhang [1,2,3] and Wenchen Feng [4]

1 Department of Thermal Engineering, Shandong Jianzhu University, Jinan 250101, China; myzhang2034@126.com (M.Z.); zhangwk10@126.com (W.Z.)
2 Key Laboratory of Renewable Energy Building Utilization Technology of Ministry of Education, Shandong Jianzhu University, Jinan 250101, China
3 Key Laboratory of Renewable Energy Building Application Technology of Shandong Province, Shandong Jianzhu University, Jinan 250101, China
4 Engineering Laboratory of Power Plant Thermal System Energy Saving of Shandong Province, Shandong University, Jinan 250061, China; prof.luantao@gmail.com (T.L.); wcfeng18@126.com (W.F.)
* Correspondence: gaoyan.sdu@hotmail.com; Tel.: +86-138-6415-4887

Received: 11 November 2018; Accepted: 7 December 2018; Published: 9 December 2018

Abstract: A series of Mn−Fe−Ce−O_x/γ-Al_2O_3 nanocatalysts were synthesized with different Mn/Fe ratios for the catalytic oxidation of NO into NO_2 and the catalytic elimination of NO_x via fast selective catalytic reduction (SCR) reaction. The effects of Mn/Fe ratio on the physicochemical properties of the samples were analyzed by means of various techniques including N_2 adsorption, scanning electron microscopy (SEM), transmission electron microscopy (TEM), X-ray diffraction (XRD), X-ray photoelectron spectroscopy (XPS), H_2-temperature-programmed reduction (TPR), NH_3-temperature-programmed desorption (TPD) and NO-TPD, meanwhile, their catalytic performance was also evaluated and compared. Multiple characterizations revealed that the catalytic performance was highly dependent on the phase composition. The Mn15Fe15−Ce/Al sample with the Mn/Fe molar ratio of 1.0 presented the optimal structure characteristic among all tested samples, with the largest surface area, increased active components distributions, the reduced crystallinity and diminished particle sizes. In the meantime, the ratios of Mn^{4+}/Mn^{n+}, Fe^{2+}/Fe^{n+} and Ce^{3+}/Ce^{n+} in Mn15Fe15−Ce/Al samples were improved, which could enhance the redox capacity and increase the quantity of chemisorbed oxygen and oxygen vacancy, thus facilitating NO oxidation into NO_2 and eventually promoting the fast SCR reaction. In accord with the structure results, the Mn15Fe15−Ce/Al sample exhibited the highest NO oxidation rate of 64.2% at 350 °C and the broadest temperature window of 75–350 °C with the NO_x conversion >90%. Based on the structure–activity relationship discussion, the catalytic mechanism over the Mn−Fe−Ce ternary components supported by γ-Al_2O_3 were proposed. Overall, it was believed that the optimization of Mn/Fe ratio in Mn−Fe−Ce/Al nanocatalyst was an extremely effective method to improve the structure–activity relationships for NO pre-oxidation and the fast SCR reaction.

Keywords: fast SCR; NO oxidation; NO_x conversion; manganese; iron; cerium

1. Introduction

Nitrogen oxides (NO_x) are one of the strong contributing factors of air pollutants, which result in acid rain, global warming and ozone depletion via photochemical redox [1]. The selective catalytic reduction (SCR) of NO_x by NH_3 or urea over high efficient catalysts is the most economical and

effective technology to eliminate the pollution of NO_x [2,3]. The main SCR reaction involves the typical standard SCR reaction (1), the fast SCR reaction (2) and the NO_2 SCR reaction (3) [4,5]:

$$4NH_3 + 4NO + O_2 \rightarrow 4N_2 + 6H_2O \quad (1)$$

$$2NH_3 + NO + NO_2 \rightarrow 2N_2 + 3H_2O \quad (2)$$

$$4NH_3 + 3NO_2 \rightarrow 3.5N_2 + 6H_2O \quad (3)$$

The catalytic mechanism of the main SCR reaction has been systematically researched during the recent years, and the reaction processes of fast SCR have also been proposed in detail [4]. Koebel et al. [6] revealed the fast SCR reaction rate was decupled larger than that of standard SCR under 200 °C. However, the typically components of NO_x were NO_2 at ~5% and NO at ~95% [2], and thus the oxidation of NO into NO_2 previous to the main SCR progress is noteworthy so as to increase the molar ratio of NO_2/NO to 1.0 for facilitating fast SCR reaction artificially.

In the SCR reaction progress, the optimized catalyst takes an important role to the NO_x removal with NH_3. The V_2O_5/TiO_2 catalyst, promoted with WO_3 or MoO_3 usually, is the most widely used commercial catalyst. The disadvantage of $V_2O_5-WO_3$ (MoO_3)/TiO_2 is the strict temperature window limit [7]. These vanadium-based catalysts are not efficient enough to eliminate NO_x as the catalytic temperature below 250 °C. In recent years, the catalysts suitable for the low temperature SCR have become required, and are appropriately installed in a downstream electrostatic precipitator and desulfurizer [8]. Many research groups dedicated to utilizing high efficient active elements and structure supports to optimize low-temperature SCR catalysts with super activities, excellent stabilities and wide-ranging temperature windows.

During the past few years, a large amount of low-temperature SCR catalysts making up of transition metal oxides on multifarious supports have been investigated. The $Mn-Fe-O_x$ based catalysts, in particular, exhibited remarkable catalytic activities, such as Mn−Fe [9], Mn−Fe/TiO_2 [10] and V_2O_5−Mn−Fe attapulgite [3]. Meanwhile, it was found that $Mn-Fe-O_x$ based catalysts could induce the oxidation reaction of NO into NO_2 during the NH_3-SCR progress [11,12]. On this basis, some researchers have recently been absorbed oxidizing NO into NO_2, due to the more high-efficiency reaction of NO_2 with NH_3 than NO [13]. Zhang et al. [13] proved the NO oxidation into NO_2 or bidentate nitrite took place on the surface of $FeMnO_x/TiO_2$ via the adsorbed oxygen. Fang et al. [14] revealed the high density of lattice oxygen in the noncrystalline $Mn-Fe-O_x$ played a leading and main role in NO oxidation. But $Mn-Fe-O_x$ based catalysts usually needed other active elements to improve their catalytic selectivity and SO_2 resistance [15]. Among various promoter, ceria performed extremely selectivity and SO_2 resistance for the low-temperature SCR in $Mn-Fe-O_x$ based catalysts [16]. At the same time, ceria as alkaline material with excellent redox abilities to adsorb and desorb active oxygen, also exhibited promoting effects on NO oxidization into NO_2 and NO_2 absorption into nitrites or nitrates [17]. However, the effects of Fe/Mn ratio on the activity of $Mn-Fe-Ce-O_x$ catalyst for NO oxidation and the fast SCR reaction have not been intensive researched, especially the combined effects of γ-Al_2O_3 as carriers. The γ-Al_2O_3 is an outstanding support material for NO oxidation due to the Brönsted acid sites on its surface besides its prominent surface area [18], remarkable mechanical strength [19], great thermal stability [1] and low production cost [20].

In this research, we systematically manufactured a series of $Mn-Fe-Ce-O_x/\gamma$-Al_2O_3 nanocatalysts with a Mn atomic ratio (Fe balance) from 0% to 100%. Their catalytic abilities of NO oxidization and the fast SCR were researched to understand the Mn/Fe ratio effects on the reactions. The physicochemical characteristics of the nanocatalyst samples were analyzed by N_2 adsorption, scanning electron microscopy (SEM) mapping, transmission electron microscopy (TEM), X-ray diffraction (XRD), X-ray photoelectron spectroscopy (XPS), H_2-temperature-programmed reduction (H_2-TPR), NH_3-temperature-programmed desorption (NH_3-TPD) and NO-TPD, in order to reveal the structure-activity relationship. The mechanism of Mn/Fe ratio influence on $Mn-Fe-Ce-O_x/\gamma$-Al_2O_3 nanocatalysts was also discussed. The purpose of this work was to clarify the nature of Mn−Fe−Ce

based materials for catalytic performance and to explore the possibility of manufacturing nanocatalysts with outstanding capabilities in both the NO oxidization into NO_2 and the fast SCR reaction progress.

2. Results and Discussion

2.1. Morphological Characterization

2.1.1. Brunauer-Emmett-Teller (BET) Measurements

In order to compare the change of physical properties of Mn−Fe−Ce−O_x/γ-Al_2O_3 nanocatalysts with different Mn/Fe ratios, the test data of BET specific surface areas, pore volumes and pore diameters were summarized in Table 1. The specific surface area and pore volume of Fe30−Ce/Al sample (Mn(x)Fe(y)−Ce/Al for short, x and y represented the mass percentage of Mn and Fe in the nanocatalysts, respectively) were originally 58.2 m^2/g and 0.33 cm^3/g, respectively. As the Mn/Fe molar ratio reached 0.5, the specific surface area rose to 77.4 m^2/g and the pore volume rose to 0.56 cm^3/g. The maximum specific surface area of 122.7 m^2/g and the maximum pore volume of 0.73 cm^3/g were both achieved over Mn15Fe15−Ce/Al with the Mn/Fe molar ratio of 1.0, which was possible due to manganese addition-enhancing active components better dispersing on the nano-Al_2O_3 support [18,21]. The manganese addition into Fe−Ce−O_x/γ-Al_2O_3 promoted mesoporosity formation and at the same time suppressed the macroporosity formation, which resulted in remarkable improvements in pore volumes [12]. Further increasing the Mn/Fe molar ratio, both the specific surface area and the pore volume started declining notably.

Table 1. Physical properties of the nanocatalysts with different Mn/Fe ratios.

Samples	BET Surface Area (m^2/g)	Pore Volume (cm^3/g)	Pore Diameter (nm)
Fe30−Ce/Al	58.2	0.33	28.76
Mn10Fe20−Ce/Al	77.4	0.56	23.84
Mn15Fe15−Ce/Al	122.7	0.73	18.06
Mn20Fe10−Ce/Al	88.2	0.54	33.60
Mn30−Ce/Al	73.3	0.50	37.99

2.1.2. Scanning Electron Microscopy (SEM), Transmission Electron Microscopy (TEM) and Mapping Analysis

The typical micrographs of SEM, TEM and Mappings of the as-prepared Mn−Fe−Ce−O_x/γ-Al_2O_3 nanocatalysts with different Mn/Fe ratios were presented in Figure 1. In the SEM images shown in Figure 1a–c, the Mn10Fe20−Ce/Al sample particles were irregular. There were lots of stacking particles distributing on the catalyst surface with abundant pores collapsing produced by the fast evaporation of crystal water [22]. While the Mn15Fe15−Ce/Al sample shaped unbroken mesoporosity mesh structure on the catalyst surface. The detailed morphology structures of Mn15Fe15−Ce/Al nanoparticle were further analyzed by TEM, as revealed in Figure 1d. The Mn15Fe15−Ce/Al sample exhibited fine uniform elliptic particles with a narrow size distribution and without hard aggregate. As the Mn/Fe molar ratio rising to 2.0, the Mn20Fe10−Ce/Al sample exhibited spinel microstructure with the nanoparticle size increasing notably. According to the element mappings of the Mn15Fe15−Ce/Al sample as displayed in Figure 1e–j, it was obvious that the corresponding components of manganese, iron and cerium species were highly dispersive on the catalyst surface without regional accumulations or crystallizations.

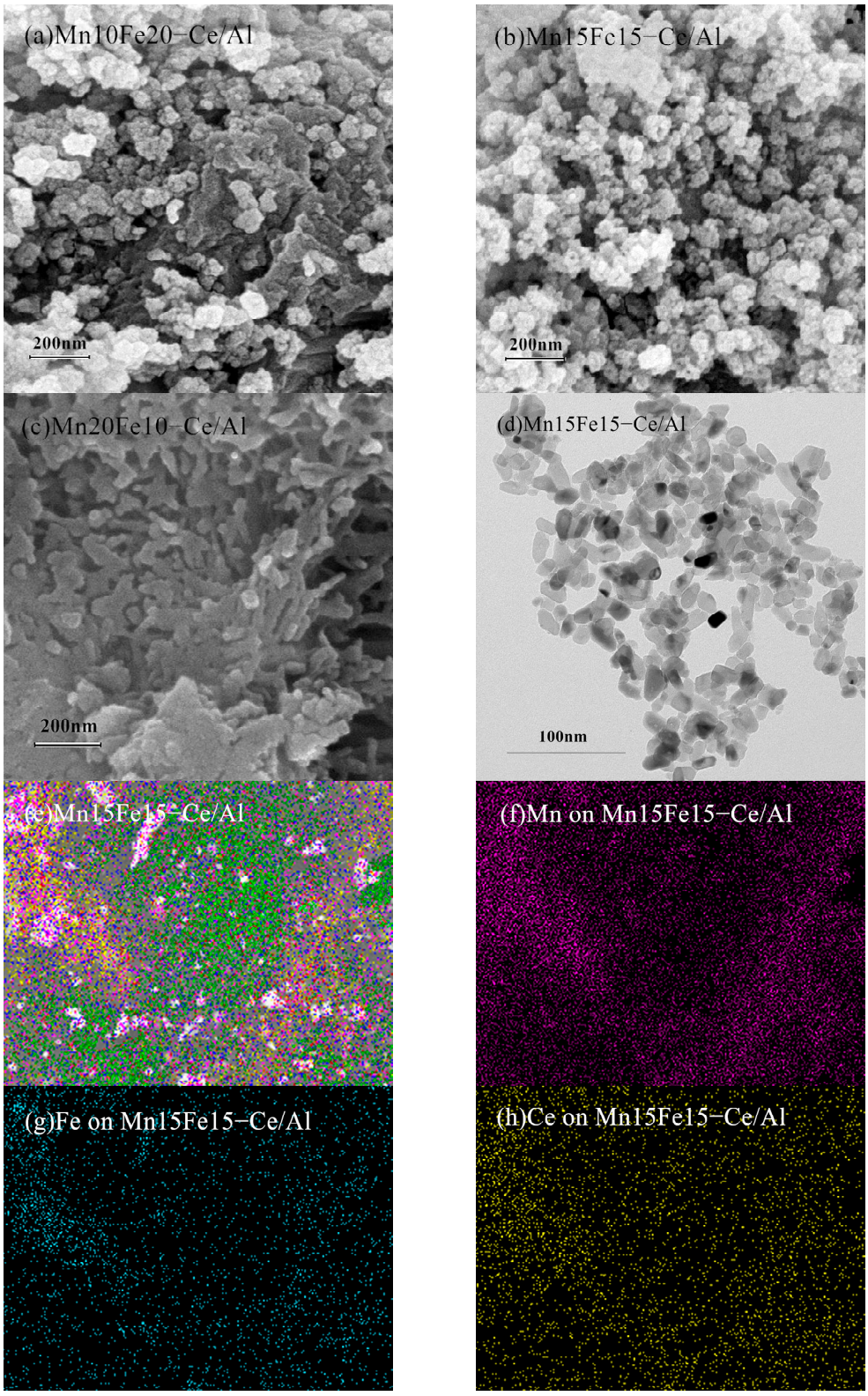

Figure 1. *Cont.*

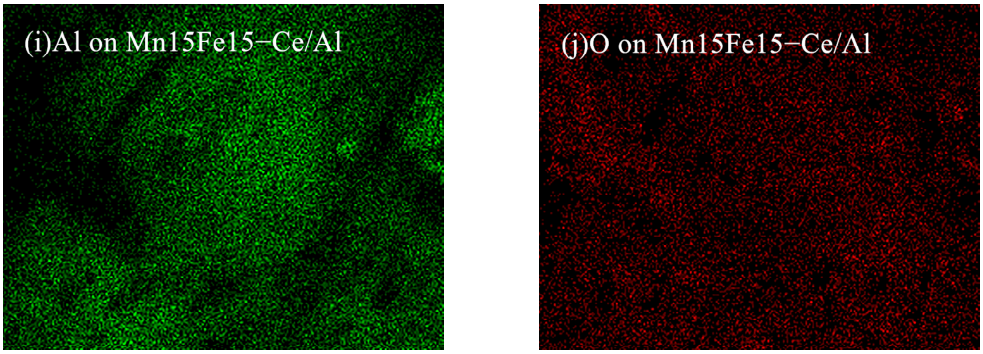

Figure 1. Scanning electron microscopy (SEM), transmission electron microscopy (TEM) and mapping of Mn−Fe−Ce−O_x/γ-Al_2O_3 nanocatalysts: (**a**) SEM of Mn10Fe20−Ce/Al; (**b**) SEM of Mn15Fe15−Ce/Al; (**c**) SEM of Mn20Fe10−Ce/Al; (**d**) TEM of Mn15Fe15−Ce/Al; (**e**) mapping of Mn15Fe15−Ce/Al; (**f**) mapping of Mn on Mn15Fe15−Ce/Al; (**g**) mapping of Fe on Mn15Fe15−Ce/Al; (**h**) mapping of Ce on Mn15Fe15−Ce/Al; (**i**) mapping of Al on Mn15Fe15−Ce/Al; (**j**) mapping of O on Mn15Fe15−Ce/Al.

2.2. Structural Characterization

2.2.1. X-Ray Diffraction (XRD) Analysis

The XRD results of Mn−Fe−Ce−O_x/γ-Al_2O_3 nanocatalysts with different Mn/Fe ratios are exhibited in Figure 2. It was obvious that the diffraction peaks in XRD patterns matched γ-Al_2O_3 with several strong and distinguished peaks at 32.3°, 37.0°, 45.3°, and 67.0° (International Centre for Diffraction Data (ICDD) PDF card # 79-1558) [23]. Although the peaks for the structure of Al_2O_3 support remained complete with different Mn/Fe molar ratios, the diffraction angles of corresponding peaks shifted towards lower angles at varying degrees. Among all tested catalysts, the Mn15Fe15−Ce/Al sample obtained the lowest diffraction angles for each peak, which manifested the potential interaction among MnO_x, FeO_x, CeO_x and Al_2O_3. For the curve of the Mn10Fe20−Ce/Al sample, the diffraction peaks coinciding with Fe_2O_3 at 2θ = 23.7°, 42.3°, 53.3°, and 63.0°, in accordance with (012), (020), (116) and (300) crystallographic plane reflections, respectively (ICDD PDF card # 88-2359) [24]. While the diffraction peaks of Fe_3O_4 or FeO were not found in the Mn10Fe20−Ce/Al sample. Comparing the curves of the Mn15Fe15−Ce/Al and Mn20Fe10−Ce/Al samples with that of Mn10Fe20−Ce/Al sample, it could be found that the diffraction peaks of Fe_2O_3 were lowered as the Mn/Fe molar ratio increased, which probably indicated the addition of manganese into Fe−Ce−O_x/γ-Al_2O_3 decreased the crystallization of Fe_2O_3. As for the Mn20Fe10−Ce/Al sample with Mn/Fe molar ratio of 2.0, the diffraction peaks coinciding with MnO_x were very complex. The characteristic peaks at 37.5°, 42.5°, 53.8°, and 64.6° could be ascribed to MnO_2 (ICDD PDF card # 89-5171), the peaks at 32.3° and 55.1° attributed to Mn_2O_3 (ICDD PDF card # 24-0508), and the peaks at 33.5°, 36.4° and 59.7° assigned to Mn_3O_4 (ICDD PDF card # 89-4837) [25]. At the same time, the peaks matched Fe_2O_3 remarkably weakened and no peaks of other FeO_x appeared.

In the curve of Mn15Fe15−Ce/Al sample, there were no evident distinct diffraction peaks of FeO_x or MnO_x were detected. These indicated the appropriate Mn/Fe molar ratio not only facilitated the dispersion of FeO_x entirely, but also enhanced the dispersion of MnO_x completely on the catalyst surface. As a result, the coexistence of iron oxides and manganese oxides increased the active species distributions, minished the particle size and reduced the crystallinity. The smaller size particles of active element species were beneficial to the fast SCR reaction [26], but the larger oxide clusters promoted NH_3 oxidation and restrained fast SCR efficiency [27]. So, the better distribution of FeO_x and MnO_x on the nanocatalyst surface had a significant impact on the fast SCR reaction. Furthermore, no evident peaks for crystalline of CeO_2 or Ce_2O_3 were observed with Mn/Fe molar ratio of 0.5~2.0 in this work, which suggested the CeO_x might be highly dispersed on the surface of Mn−Fe−Ce/Al or the crystal diameters of CeO_x were too small (<5 nm) to be distinguished.

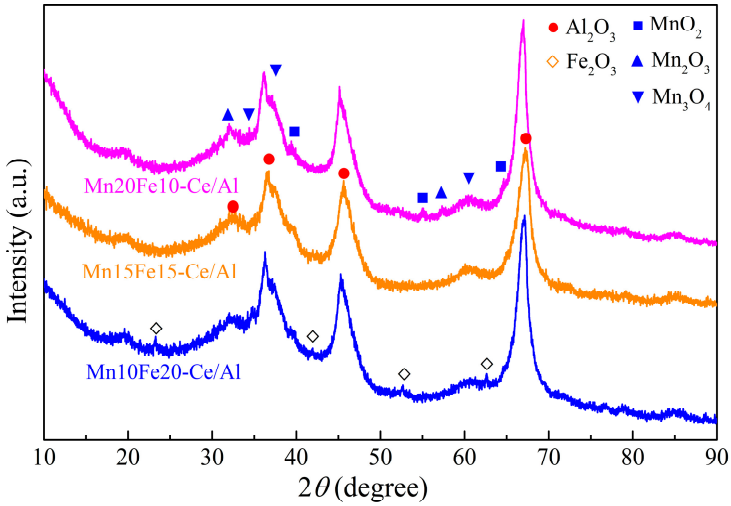

Figure 2. X-ray diffraction (XRD) patterns of Mn−Fe−Ce−O_x/γ-Al_2O_3 nanocatalysts.

2.2.2. X-Ray Photoelectron Spectroscopy (XPS) Analysis

In fast SCR reaction, the components of catalyst surface and the oxidation states of active species had significant effects on the catalytic activity [5]. For the purpose of exploring the atomic chemical valences and revealing the element concentrations on the catalyst surface, XPS analysis of Mn−Fe−Ce−O_x/γ-Al_2O_3 nanocatalysts was undertaken. The XPS spectra of Mn 2*p*, Fe 2*p*, Ce 3*d*, and O 1*s* in the nanocatalysts were exhibited in Figure 3. The valence states of each element were confirmed numerically by Gaussian fitting, respectively. According to these fittings, the relevant binding energy and the respective atomic concentration of elements in diverse valence states on Mn−Fe−Ce−O_x/γ-Al_2O_3 surface are shown in Table 2.

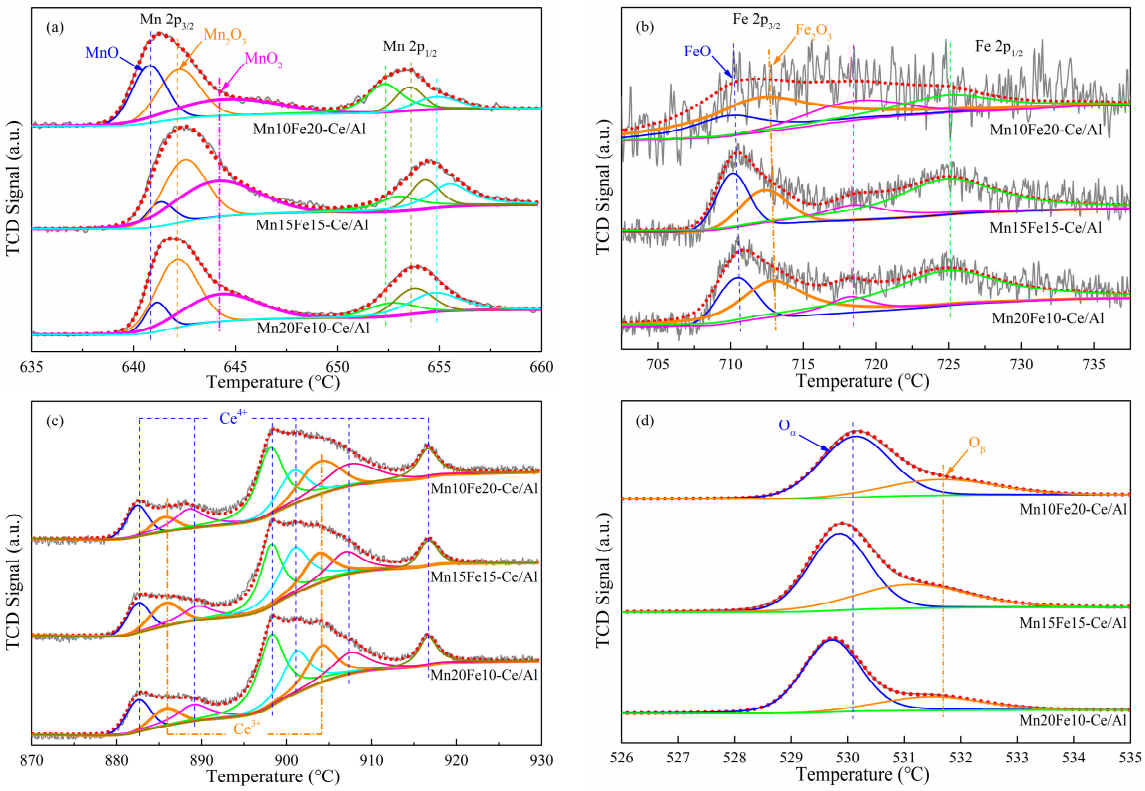

Figure 3. X-ray photoelectron spectroscopy (XPS) analysis of Mn−Fe−Ce−O_x/γ-Al_2O_3 nanocatalysts: (**a**) XPS spectra for Mn 2*p*; (**b**) XPS spectra for Fe 2*p*; (**c**) XPS spectra for Ce 3*d*; (**d**) XPS spectra for O 1*s*.

Table 2. Surface atomic compositions of the catalysts determined by XPS.

Samples	Binding Energy (eV)/Atomic Composition (%)								
	Mn			Fe		Ce		O	
	Mn^{2+} $2p_{3/2}$	Mn^{3+} $2p_{3/2}$	Mn^{4+} $2p_{3/2}$	Fe^{2+} $2p_{3/2}$	Fe^{3+} $2p_{3/2}$	Ce^{3+} $3d_{5/2}$	Ce^{4+} $3d_{5/2}$	O_α $1s$	O_β $1s$
Mn10Fe20−Ce/Al	640.8/33.9	642.1/36.2	644.1/29.9	709.8/28.1	712.0/71.9	885.819.4	882.6/80.6	530.3/76.6	531.7/23.4
Mn15Fe15−Ce/Al	641.3/6.8	642.5/39.4	644.4/53.8	709.1/52.4	711.3/47.6	885.5/33.8	882.4/66.2	529.7/62.6	531.2/37.4
Mn20Fe10−Ce/Al	641.1/12.7	642.247.2	644.2/40.1	709.4/42.7	711.8/57.3	885.7/23.8	882.5/76.2	529.4/70.2	531.3/29.8

It can be seen from Figure 3a that the XPS spectra of Mn $2p$ in the investigated nanocatalyst samples were matched with two constituents, attributed to Mn $2p_{3/2}$ (peak at around 642 eV) and Mn $2p_{1/2}$ (peak at about 653 eV) existing in MnO_x simultaneously [28]. The dissymmetric peak of Mn $2p_{3/2}$ further confirmed the complex co-existence of manganese species in various states. The spectra of Mn $2p_{3/2}$ could be split into three peaks via the peak-fitting deconvolution. As reported in previous studies [22], the first peak at around 641.0 ± 0.3 eV associated with MnO, the second one at 642.2 ± 0.3 eV is consistent with Mn_2O_3, and the third one at 644.2 ± 0.3 eV was assigned to MnO_2, respectively. It was apparent that the three valence states of MnO_x were difficult to separate within the binding energy difference value of 3.3 eV. The surface atomic compositions and relative intensities of Mn^{n+} on the catalyst surface were calculated on account of the area covered under the separated peaks, as summarized in Table 2. With the Mn/Fe molar ratio increasing from 0.5 to 1.0, the Mn^{2+} concentration on the sample surface reduced obviously from 33.9% to 6.8%; by contrast, the concentration of Mn^{4+} rose significantly from 29.9% to 53.8% which became larger than that of Mn^{3+}. From the above results, it was proposed that the principal phase of manganese species in the Mn−Fe−Ce−O_x/γ-Al_2O_3 nanocatalysts changed from Mn_2O_3 to MnO_2. This was also possibly ascribed to the major amount of Mn mainly existing as +4 state covering dispersedly on the catalyst surface. Keeping on increasing the Mn/Fe molar ratio to 2.0, the percentage of Mn^{4+} in Mn^{n+} began to decline, at the same time the Mn^{3+}/Mn^{n+} ratio increased remarkably. The NO catalytic activity of pure manganese oxides had been ranked as $MnO_2 > Mn_2O_3 > Mn_3O_4$ [25]. Furthermore, there were studies revealed that the increased concentration of Mn^{4+} on the catalyst surface was beneficial to SCR reactions [29]. Consequently, it could be expected that the Mn15Fe15−Ce/Al nanocatalyst would provide a superior fast SCR activity compared to Mn10Fe20−Ce/Al and Mn20Fe10−Ce/Al samples.

The Fe $2p$ XPS spectra of Mn−Fe−Ce−O_x/γ-Al_2O_3 nanocatalysts are displayed in Figure 3b with two distinctive peaks presented for Fe $2p_{3/2}$ (709.1–712.0 eV) and Fe $2p_{1/2}$ (723.8–725.0 eV). The broad peak centered at 711.0 eV included two overlapped peaks, the first one at about 709.4 ± 0.4eV was related to Fe^{2+} and the second one at around 711.8 ± 0.5eV was ascribed to Fe^{3+}. Meanwhile, a satellite peak of Fe^{3+} in Fe_2O_3 appeared at 718.4 eV [10]. The overlapping peaks manifested the coexistence of iron in +2 and +3 states on the catalyst surface, which were quantified in Table 2. With the Mn/Fe molar ratio increasing from 0.5 to 1.0, the percentage of Fe^{3+} in Fe^{n+} decreased, while the Fe^{2+} concentration was improved. These could be attributed to the synergistic effects taking place in the redox equilibrium between Fe and Mn: $Fe^{3+} + Mn^{3+} \leftrightarrow Fe^{2+} + Mn^{4+}$ [30].

Figure 3c showed the Ce $3d$ spectra results for Mn−Fe−Ce−O_x/γ-Al_2O_3 nanocatalysts. The Ce $3d$ curve contained u and v multiplets conforming to the spin orbit split $3d_{5/2}$ and $3d_{3/2}$ core holes, which were further split into eight peaks on the basis of binding energy, labeled as u^0, u', u'', u''' and v^0, v', v'', v''', respectively [31]. The two peaks labeled u' and v' were attributed to the $3d^{10}4f^1$ initial electronic state of Ce^{3+}, and the other six bands corresponded to the $3d^{10}4f^0$ state of Ce^{4+} [32]. These indicated the species of Ce^{3+} and Ce^{4+} coexisted on the surface of Mn−Fe−Ce−O_x/γ-Al_2O_3 nanocatalysts. As shown in Table 2, it was obvious that the Ce^{3+}/Ce^{n+} ratio of Mn15Fe15−Ce/Al sample was 33.8%, as calculated by Equation (4) [33], which was greater than that of the other two catalyst samples. Therefore, the Mn/Fe molar ratio of 1.0 might be positive to the conversion from Ce^{4+} to Ce^{3+}, which resulted in an improvement of Ce^{3+} species on its surface.

$$\eta_{Ce^{3+}} = \frac{u' + v'}{u^0 + u' + u'' + u''' + v^0 + v' + v'' + v'''} \times 100\% \quad (4)$$

The generated species of Ce^{3+} were significant inducements for the formation of electric charge balance, the generation of unsaturated chemical bonds, the improvement of surface oxygen vacancies, and the development of more chemisorbed oxygen, which would be advantageous to the activate reactants adsorption or intermediate species transformations [5]. As the temperature was under 200 °C, the main catalytic reactions followed the Eley–Rideal mechanism. NH_3 absorbed on active sites to generate NH_2 and −OH with oxygen. Subsequently, the achieved NH_2 further reacted with NO forming intermediate NH_2NO, and finally the intermediate species decomposed into N_2 and H_2O [34]. Thus, it was proposed that the quantity improvement of oxygen vacancies on the catalyst was conducive to facilitating the intermediate formation and enhancing catalytic performance in the fast SCR reaction. In the crystal lattice of Mn15Fe15−Ce/Al sample, the negative charge transferred from manganese to cerium intensifying the interaction between Mn and Ce: $Mn^{2+} + Ce^{4+} \leftrightarrow Mn^{3+} + Ce^{3+}$ [16,35], $Mn^{3+} + Ce^{4+} \leftrightarrow Mn^{4+} + Ce^{3+}$ [36,37]. The course of oxygen storage and release on the Ce^{3+}/Ce^{4+} redox couple was brought forward: $Ce_2O_3 + 1/2O_2 \rightarrow 2CeO_2$ and $2CeO_2 \rightarrow Ce_2O_3 + O^*$ (adsorbed) [36]. Overall, it could be easier for the catalysts with more Ce^{3+} species on the surface to develop surface oxygen vacancies, which was beneficial to the oxygen adsorption to achieve chemisorbed oxygen [10].

The XPS spectra of O 1*s* for Mn−Fe−Ce−O_x/γ-Al_2O_3 nanocatalysts are illustrated in Figure 3d. According to the curve-fitting results, the O 1*s* spectra was split into two peaks: the first peak labeled by O_α was ascribed to lattice oxygen appearing at binding energy of 529.5–530.3 eV, the second peak denoted as O_β was attributed to chemisorbed oxygen on the catalyst surface at the binding energy of 531–532 eV. Compared with the XPS spectra of the Mn10Fe20−Ce/Al sample, both binding energies of O_α and O_β in the Mn15Fe15−Ce/Al and Mn20Fe10−Ce/Al samples shifted towards lower values, which might be caused by the existence of more Mn^{4+} species [9]. Furthermore, the surface concentration of chemisorbed oxygen of the Mn15Fe15−Ce/Al sample reached 37.4% as shown in Table 2, which was much larger than that of the Mn10Fe20−Ce/Al and Mn20Fe10−Ce/Al samples. The chemisorbed oxygen with high mobility was regard as the most active oxygen species in the SCR process, facilitating NO oxidation to NO_2 and promoting the fast SCR reaction in the gas mixture: $NO + NO_2 + 2NH_3 \rightarrow 2N_2 + 3H_2O$ [4].

2.2.3. H_2-Temperature-Programmed Reduction (H_2-TPR) Analysis

The reduction behavior of Mn−Fe−Ce−O_x/γ-Al_2O_3 nanocatalysts were analyzed by H_2-TPR and the curves were matched by Gaussian functions as shown in Figure 4. For each of the three nanocatalyst samples, there were five main hydrogen consumption peaks locating in the range from 100 to 900 °C. Since the support of alumina had no obvious H_2 consumption peaks in the temperature range [38], all the peaks exhibited in Figure 4 could be associated with the reduction of different species of MnO_x, FeO_x and CeO_x. For Mn10Fe20−Ce/Al sample, the initial wider reduction peak (P1) from 160 °C to 440 °C was assigned to the high oxidation state of manganese ion transformation from MnO_2 reducing to Mn_2O_3 [15]. Considering the existence of Fe_2O_3 crystallization had been confirmed by XRD analysis, the second prominent reduction peak (P2) centered at 366 °C could be mainly attributed to Mn_2O_3 species combining with the majority of Fe_2O_3 to Fe_3O_4, where iron species were settled in easily reducible sites in the form of isolated ions, oligomeric clusters or nanoparticles [39]. According to a previous report [40], the Mn_2O_3 reduction consists of two processes, Mn_2O_3 to Mn_3O_4 and Mn_2O_3 to MnO. The reduction from Mn_2O_3 to Mn_3O_4 happened more easily on the initial amorphous Mn_2O_3, and the conversion from Mn_2O_3 to MnO occurred more easily at the higher temperature range. Therefore, the third reduction peak (P3) centered at 434 °C was due to the reduction process of Mn_2O_3 to MnO and the reduction of residual Fe_2O_3 to Fe_3O_4. Meanwhile, the fourth reduction peak (P4) at around 643 °C and the fifth one (P5) at approximately 761 °C were potentially associated with the reduction process of Fe_3O_4 to FeO and FeO to Fe^0 in isolated ions, respectively [41].

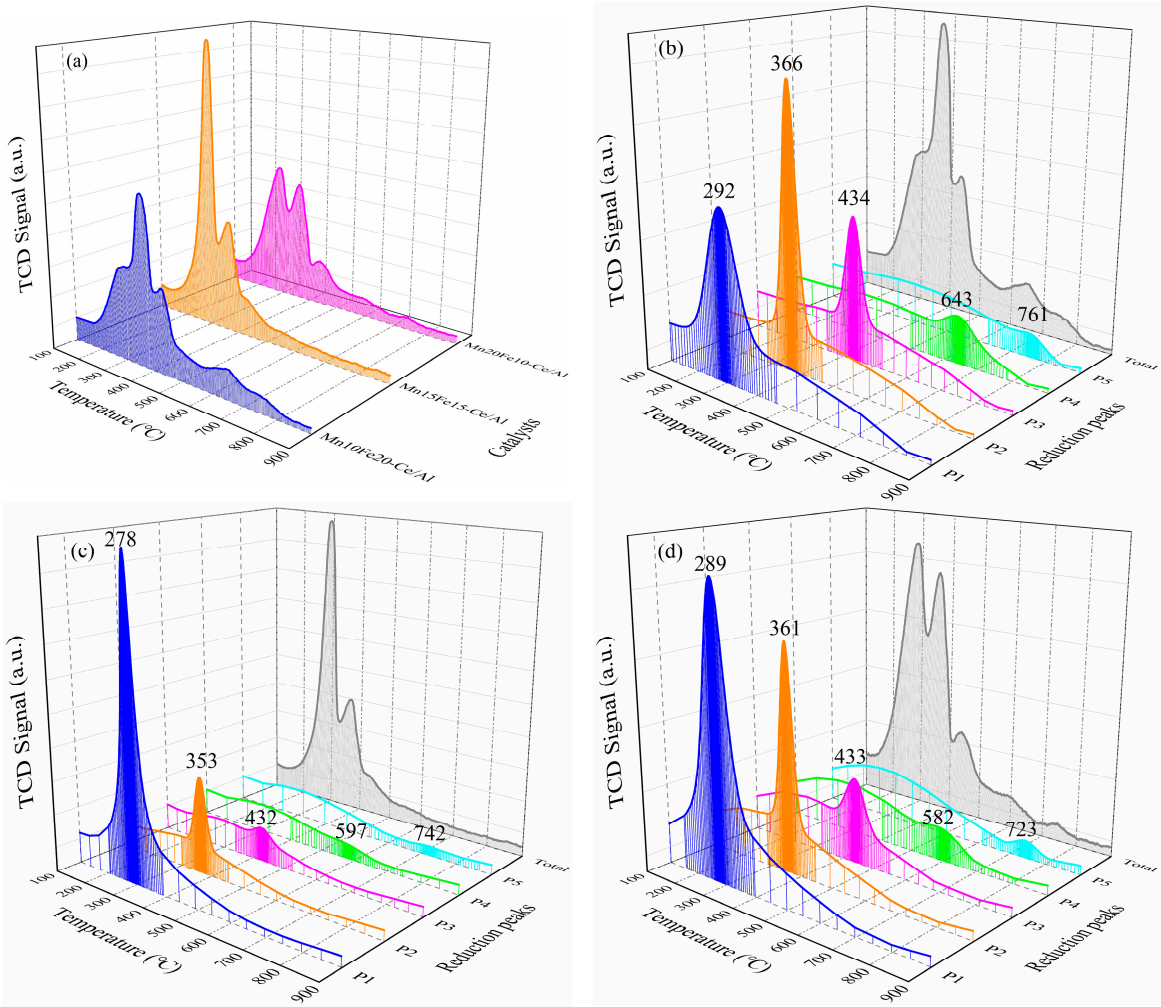

Figure 4. H_2-temperature-programmed reduction (H_2-TPR) profiles of Mn−Fe−Ce−O_x/γ-Al_2O_3 nanocatalysts: (**a**) total H_2-TPR curves; (**b**) multi-peak Gaussian fitting for Mn10Fe20−Ce/Al sample; (**c**) multi-peak Gaussian fitting for Mn15Fe15−Ce/Al sample; (**d**) multi-peak Gaussian fitting for Mn20Fe10−Ce/Al sample.

In comparison, the redox characteristic of Mn15Fe15−Ce/Al sample was significantly different from that of Mn10Fe20−Ce/Al sample. The H_2-TPR curve of Mn15Fe15−Ce/Al sample exhibited as a disequilibrium bimodal pattern, and the two main reduction peaks were at around 279 °C and 353 °C, respectively. It was rather remarkable that the MnO_2 reduction peak and the Fe_2O_3 reduction peak varied drastically with the Mn/Fe molar ratio increasing from 0.5 to 1.0. As shown in Figure 4c, the increasing Mn/Fe molar ratio resulted in the significant promotion of reducibility at a low temperature range. The reduction peak P1 was much stronger and broader with the hydrogen consumption maximum obtained at a lower temperature region. Comparing the H_2-TPR curves of Mn15Fe15−Ce/Al sample with that of Mn10Fe20−Ce/Al sample, it was noteworthy that all the reduction peaks of MnO_x and FeO_x shifted towards the lower temperature regions, signifying enhanced catalytic activities at lower temperature. Similar results were achieved by Wang et al. [12] that confirmed the Mn–Fe mixtures leading to lower temperature for Fe_3O_4 reducing to FeO and FeO converting to Fe^0 at the same time. However, as the Mn/Fe molar ratio increased to 2.0 in the Mn20Fe10−Ce/Al sample, the reduction peaks involving MnO_x and FeO_x (P1, P2 and P3) moved to higher temperature section slightly, while the reduction peaks only containing FeO_x (P4 and P5) still shifted towards lower temperature region. In consideration of the crystallization of MnO_2, Mn_2O_3 and Mn_3O_4 observed in the XRD results as shown in Figure 2, it was supposed that the actual Mn/Fe

molar ratio in the $MnFeO_x$ nano particle was reduced, and the dominant reduction peak P1 was mainly caused by the reduction of crystallographic MnO_2 [11,30].

The redox ability of Mn−Fe−Ce−O_x/γ-Al_2O_3 nanocatalysts could be determined by the starting reduction peak temperature [42], which followed the order of Mn15Fe15−Ce/Al > Mn20Fe10−Ce/Al > Mn10Fe20−Ce/Al. This indicated that the suitable Mn/Fe molar ratio enhanced the redox activities of MnO_x and FeO_x, and was further confirmed by the total H_2 consumption as shown in Table 3. As the Mn/Fe molar ratio increased from 0.5 to 2.0, the total H_2 consumption rose from 4.93 mmol/g to 6.11 mmol/g, and then declined to 5.97 mmol/g. On account of the redox property being an important factor affecting the fast SCR reaction, it was reasonable that the Mn15Fe15−Ce/Al sample exhibited higher NO oxidation rate and fast SCR reaction activity than the Mn20Fe10−Ce/Al and Mn10Fe20−Ce/Al samples. Meanwhile, it could be noticed that there were no distinguishable reduction peaks corresponds to cerium species. According to previous research [43], the typical reduction peaks at around 450 °C and 740 °C could be associated with the surface Ce^{4+} converting to Ce^{3+} and the bulk Ce^{4+} transforming to Ce^{3+}, respectively. In this work, the reduction peaks of cerium species were very weak due to the low-quality content of cerium. At the same time, the characteristic reduction peaks of cerium were overlapped with the reduction process of Mn_2O_3 to MnO and Fe_2O_3 to Fe_3O_4 at 380~500 °C (P3), and covered by the FeO to Fe^0 reduction at 700~800 °C (P5). Figure 5 provides a graphical representation of the reduction process, in which each active component is embodied qualitatively.

Overall, on the basis of the reduction process analyzed above, the optimal Mn/Fe molar ratio for Mn−Fe−Ce−O_x/γ-Al_2O_3 nanocatalysts was 1.0 with increased H_2 consumption and lower reduction peak temperature. This indicated that the reinforced reducibility in Mn15Fe15−Ce/Al sample was potentially due to the strong interaction between MnO_x and FeO_x with the best material proportion.

Table 3. Quantitative analysis of H_2-TPR profiles.

Samples	Temperature (°C)/H_2 Consumption (mmol/g)					
	Peak 1	Peak 2	Peak 3	Peak 4	Peak 5	Total
Mn10Fe20−Ce/Al	292/1.45	366/2.30	434/0.80	643/0.27	761/0.11	–/4.93
Mn15Fe15−Ce/Al	278/4.86	353/0.85	432/0.16	597/0.14	742/0.10	–/6.11
Mn20Fe10−Ce/Al	289/2.92	361/2.13	433/0.51	582/0.28	723/0.13	–/5.97

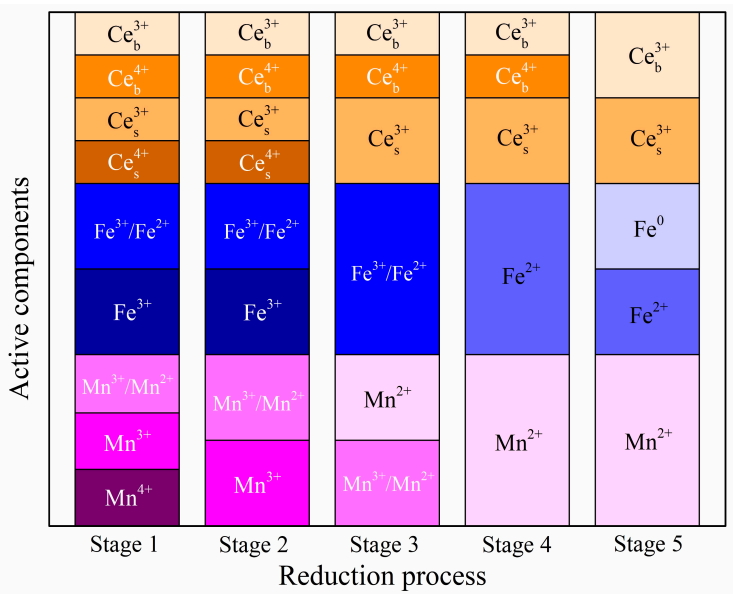

Figure 5. Graphical representation of the reduction process of Mn−Fe−Ce−O_x/γ-Al_2O_3 nanocatalysts with the reduction agent of H_2 from 100 to 900 °C.

2.2.4. NH_3-Temperature-Programmed Desorption (NH_3-TPD) and NO-TPD Analysis

Except for the satisfactory redox behavior, it was another pivotal factor that the acid sites on the catalyst surface were sufficient to enhance the catalytic activities in the SCR reaction [9,17]. For the purpose of intensive investigation of the complicated relationship between the surface acidity and the activities, NH_3-TPD and NO-TPD experiments were performed on Mn−Fe−Ce−O_x/γ-Al_2O_3 nanocatalysts and the corresponding curves according to data analysis were showed in Figures 6 and 7, respectively. The NH_3-TPD patterns for these catalysts were ascribed to three desorption peaks of chemisorbed NH_3 in the temperature range from 120 to 700 °C. For the Mn10Fe20−Ce/Al sample, the first weak peak (P1) was ranged at around 213 °C, which was attributed to NH_3 desorption from the weak acid sites. The second stronger peak (P2) positioned at about 383 °C approximately was ascribed to the medium-strong acid sites. The third dominating desorption peak (P3) at around 547 °C signified the distribution of strong acid sites, which exhibited a large amount of strong acid sites matching to the desorption of strongly bound ammonia on the potential Lewis acid sites [44]. Compared with the NH_3-TPD pattern of the Mn10Fe20−Ce/Al sample, the Mn15Fe15−Ce/Al sample displayed superior acidity property at the medium- and low-temperature regions, where all the three desorption peaks shifted towards lower temperatures and converted to much wider spans. The enhancements of medium-strong acid sites and weak acid sites were positive to ammonia adsorption, which was proposed that NH_3 probably adsorbed on both Lewis acid sites and Brönsted acid sites on the catalyst surface [12]. As the Mn/Fe molar ratio increased to 2.0 in the Mn20Fe10−Ce/Al sample, the NH_3 desorption peaks moved further to the lower temperature region, and meanwhile the two strong peaks of medium-strong acid sites and weak acid sites became overlapped from 150 °C to 450 °C. The desorption peak of strong acid sites apparently reduced, which would be the reason for the decrease in fast SCR activity of Mn20Fe10−Ce/Al sample.

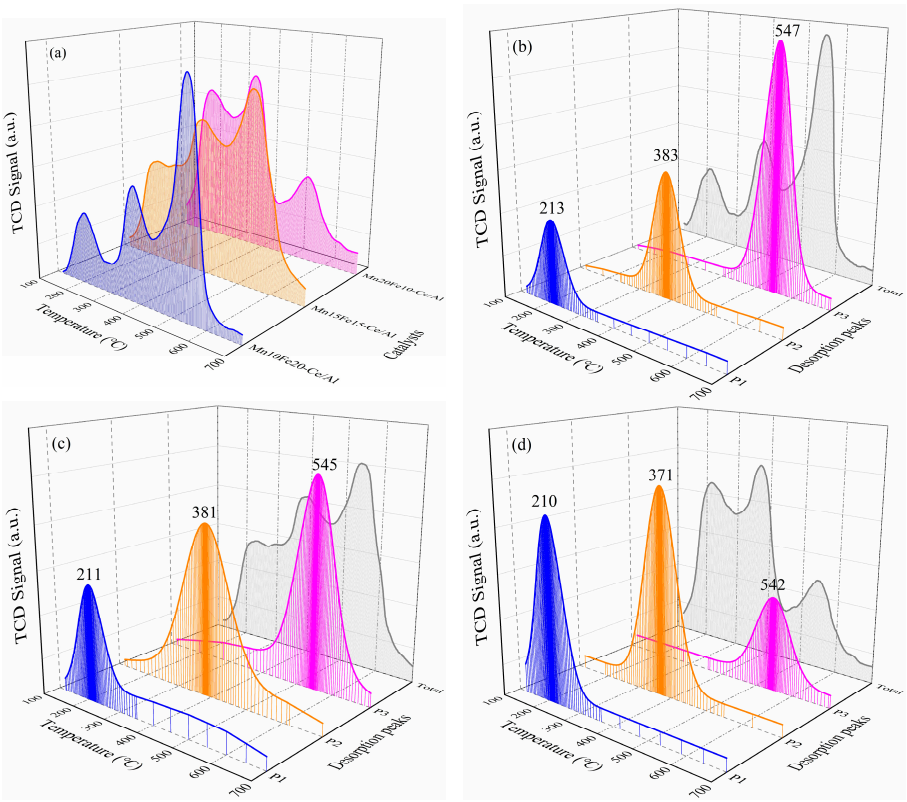

Figure 6. NH_3-temperature-programmed desorption (NH_3-TPD) profiles of Mn−Fe−Ce−O_x/γ-Al_2O_3 nanocatalysts: (**a**) total NH_3-TPD curves; (**b**) multi-peak Gaussian fitting for Mn10Fe20−Ce/Al sample; (**c**) multi-peak Gaussian fitting for Mn15Fe15−Ce/Al sample; (**d**) multi-peaks Gaussian fitting for Mn20Fe10−Ce/Al sample.

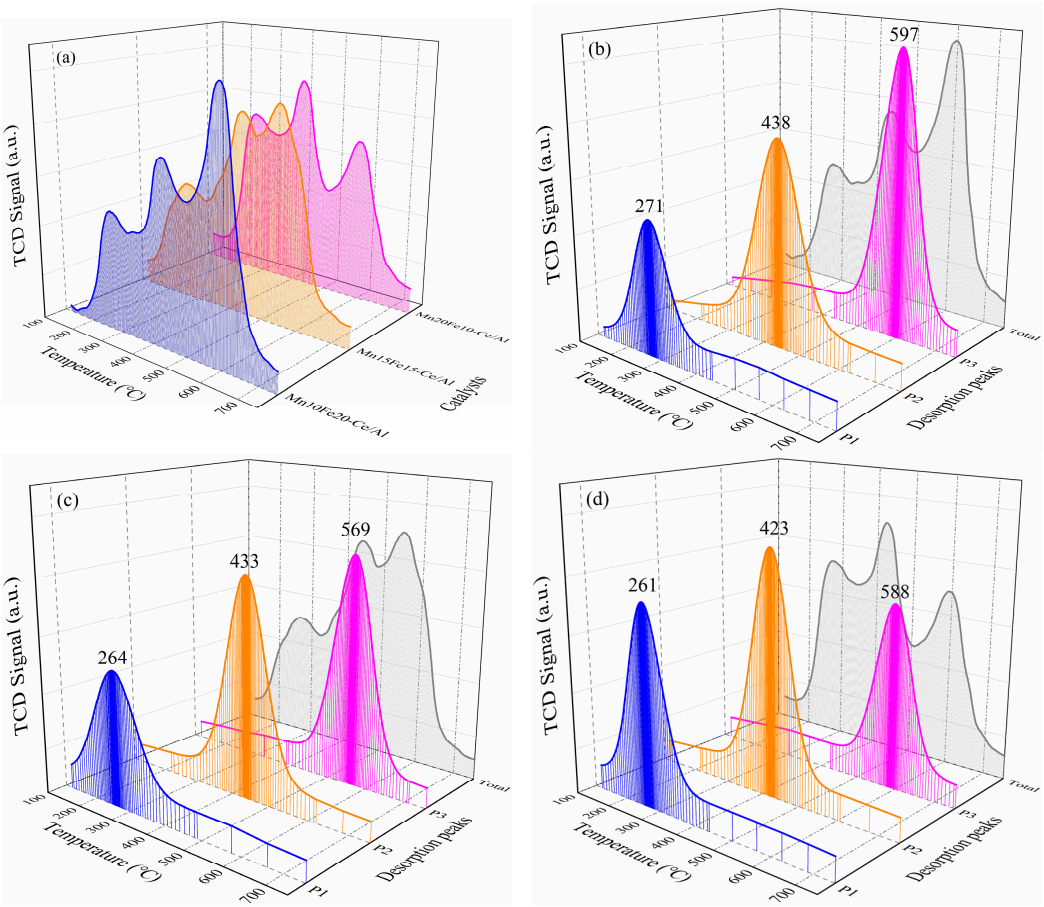

Figure 7. NO-temperature-programmed desorption (NO-TPD) profiles of Mn−Fe−Ce−O_x/γ-Al_2O_3 nanocatalysts: (**a**) total NO-TPD curves; (**b**) multi-peak Gaussian fitting for Mn10Fe20−Ce/Al sample; (**c**) multi-peak Gaussian fitting for Mn15Fe15−Ce/Al sample; (**d**) multi-peak Gaussian fitting for Mn20Fe10−Ce/Al sample.

For the purpose of accurately analyzing the total surface acidity, the desorption peaks of the Mn10Fe20−Ce/Al, Mn15Fe15−Ce/Al and Mn20Fe10−Ce/Al samples were quantitatively analyzed and are summarized in Table 4. The total NH_3 consumption grew from 1.24 mmol/g to 1.61 mmol/g with the Mn/Fe molar ratio increasing from 0.5 to 1.0, which further confirmed the promotion effects of the Mn/Fe molar ratio on the surface acidity of nanocatalyst samples. These could be explained by the creation of more Brönsted acid sites on the catalyst surface [16]. It was noteworthy that the Mn20Fe10−Ce/Al sample exhibited the best acidity properties at the low temperature, 0.56 mmol/g at 210 °C, which was beneficial to ammonia adsorption and advantageous to the low-temperature SCR reaction. However, it was found that the blocking effects of NH_3 applied especially to the fast SCR reaction at low temperatures [45]. The inhibiting effects were probably due to a competition of NH_3 with NO for adsorption and activation onto the metal oxidizing centers on the catalyst surface, and a disadvantageous electronic interaction between the adsorbed NH_3 and the metal sites [46]. As such, the acidity property on the nanocatalyst surface was closely associated with the redox behavior. In order to obtain the optimal catalyst, it was desirable to seek an appropriate equilibrium among the surface components, the oxidation states of metal species and the acidity property.

It was obvious that the NO-TPD patterns of Mn−Fe−Ce−O_x/γ-Al_2O_3 nanocatalysts as shown in Figure 7 are quite similar to the NH_3-TPD patterns discussed above. With temperature rising from 120 to 750 °C, each of the three catalyst samples exhibited three desorption peaks of chemisorbed NO. The dominating desorption peak of Mn10Fe20−Ce/Al sample was at about 597 °C attributed to the strong Lewis acid sites. While the main desorption peaks of Mn15Fe15−Ce/Al and Mn20Fe10−Ce/Al

samples were settled at around 420~430 °C, which were ascribed to the overlapped peaks of Lewis acid sites and Brönsted acid sites. With the Mn/Fe molar ratio increasing from 0.5 to 2.0, the NO desorption at low temperature apparently augmented from 0.32 mmol/g to 0.59 mmol/g, while NO desorption in the high-temperature region declined from 0.70 mmol/g to 0.39 mmol/g, which was supposed to be conducive to fast SCR at low temperature [17].

Table 4. Quantitative analysis of NH_3-TPD profiles.

Samples	Temperature (°C)/NH_3 Composition (mmol/g)				Temperature (°C)/NO Composition (mmol/g)			
	Peak 1	Peak 2	Peak 3	Total	Peak 1	Peak 2	Peak 3	Total
Mn10Fe20−Ce/Al	213/0.16	383/0.32	547/0.76	−/1.24	271/0.32	438/0.56	597/0.70	−/1.58
Mn15Fe15−Ce/Al	211/0.38	381/0.68	545/0.55	−/1.61	264/0.44	433/0.67	569/0.64	−/1.75
Mn20Fe10−Ce/Al	210/0.56	371/0.71	542/0.29	−/1.56	261/0.59	423/0.69	588/0.39	−/1.67

2.3. Fast SCR Activity of Mn−Fe−Ce−O_x/γ-Al_2O_3

2.3.1. Effect of Mn/Fe Ratio on NO Oxidation of NO_2

The reaction of NO oxidation into NO_2 on Mn−Fe−Ce−O_x/γ-Al_2O_3 nanocatalysts with different Mn/Fe molar ratios are exhibited in Figure 8. Pure MnO_2 or Fe_2O_3 doping on CeO_x/γ-Al_2O_3 was also studied for comparison. It was easy to see that the NO oxidation of the five tested catalyst samples improved prominently with the temperature increasing from 25 °C to 350 °C. The NO oxidation of Fe30−Ce/Al sample was only less than 5% below 150 °C. The addition of Mn species into Fe−Ce−O_x/γ-Al_2O_3 increased the NO oxidation rate obviously and expanded the lower temperature window particularly. It was obvious that the Mn15Fe15−Ce/Al sample, which comprised the best Mn/Fe molar ratio, displayed the highest oxidation ability among the tested catalysts with the NO oxidation reaching approximately 31.3% at 150 °C and 64.2% at 350 °C, respectively. As the temperature rose above 350 °C, the NO oxidation rates began to decrease significantly for all tested samples. Moreover, the Mn20Fe10−Ce/Al and Mn30−Ce/Al samples showed lower NO oxidation rate than that of Mn15Fe15−Ce/Al sample in the researched temperature window. For the Mn20Fe10−Ce/Al sample, there was a noteworthy morphological transformation on the catalyst surface, as shown in Figure 1c, and the characteristic peaks of MnO_2, Mn_2O_3 and Mn_3O_4 appeared obvious in the XRD curve as exhibited in Figure 2. Hence, it could be confirmed that the higher crystallization of MnO_x was one of the main reasons for the deterioration of NO oxidation with Mn20Fe10−Ce/Al_2O_3 catalyst.

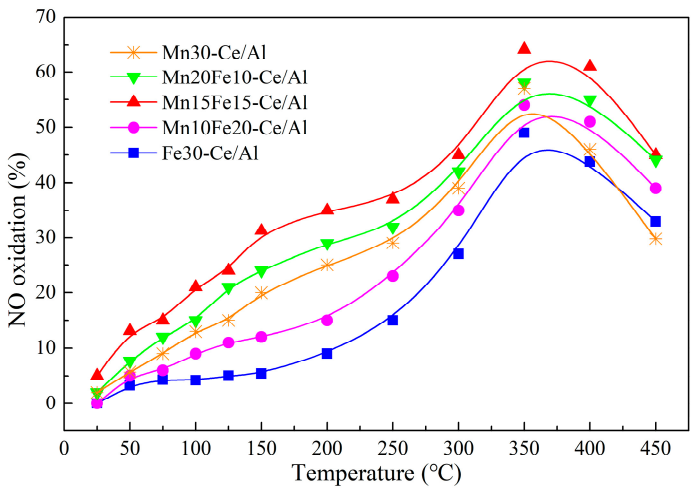

Figure 8. The activity of NO oxidation into NO_2 over Mn−Fe−Ce−O_x/γ-Al_2O_3 nanocatalysts.

2.3.2. Effect of Mn/Fe Ratio on fast SCR Activity

The fast SCR activity of the prepared Mn−Fe−Ce−O_x/γ-Al_2O_3 nanocatalysts with diverse Mn/Fe molar ratios at different reaction temperatures were illustrated in Figure 9. It was found that the Mn/Fe molar ratio had remarkable effects on the catalytic performances of Mn−Fe−Ce−O_x/γ-Al_2O_3 nanocatalysts. Among all analyzed catalyst samples, the Mn15Fe15−Ce/Al sample exhibited the highest fast SCR activity in the whole tested temperature window, with NO_x conversion above 90% at 75–350 °C. As illustrated in Figure 9a, the Fe30−Ce/Al sample showed the lowest catalytic activity in NO_x conversion with the temperature rising from 25 °C to 200 °C. The addition of Mn into Fe−Ce/Al sample enhanced the fast SCR activity obviously. The appropriate amount of Mn doping enhanced the catalytic activity, while the excessive Mn doping caused a negative impact. When the Mn/Fe molar ratio grew to 0.5, the NO_x conversion of Mn10Fe20−Ce/Al sample achieved approximately 90.3% at 150 °C. When the Mn/Fe molar ratio was larger than 1.0, the NO_x conversion of Mn20Fe10−Ce/Al and Mn30−Ce/Al samples began to decline slightly. However, as the temperature changed within 250–350 °C, the variation tendency of NO_x conversion with the Mn/Fe molar ratios increasing were entirely different. In the high temperature range, the Mn30−Ce/Al sample showed the lowest catalytic activity in NO_x conversion, and the Mn20Fe10−Ce/Al sample had as high a catalytic activity as Mn15Fe15−Ce/Al. The reduction of NO_x conversion was caused by the non-selective oxidation of NH_3 at high temperatures, which was probably due to the redox property enhancement produced by manganese addition [47]. Moreover, the NO conversion performance of Mn−Fe−Ce−O_x/γ-Al_2O_3 nanocatalysts was similar to that of NO_x conversion according to Figure 9b.

The NO_2 conversion of Mn−Fe−Ce−O_x/γ-Al_2O_3 nanocatalysts could be divided into two phases as shown in Figure 9c. As the temperature below 200 °C, the NO_2 conversion of all tested catalysts improved with the temperature increasing. In this temperature range, the NO_2 conversion of Mn−Fe−Ce−O_x/γ-Al_2O_3 nanocatalysts raised initially and then reduced with the Mn/Fe molar ratio increasing. The highest NO_2 conversion was obtained over the Mn15Fe15−Ce/Al sample with the Mn/Fe molar ratio of 1.0. As the temperature above 200 °C, the NO_2 conversion of all tested catalysts stabilized at approximately 99%. Based on the Figure 9, the fast SCR activity of Mn−Fe−Ce−O_x/γ-Al_2O_3 nanocatalysts could be ranked Fe30−Ce/Al < Mn10Fe20−Ce/Al < Mn30−Ce/Al < Mn20Fe10−Ce/Al < Mn15Fe15−Ce/Al. Generally, the variation tendency of the specific surface area and the pore volume with the Mn/Fe molar ratio increasing coincided with that of fast SCR activity. Thereby, it could be believed that the fast SCR activity of Mn−Fe−Ce−O_x/γ-Al_2O_3 nanocatalysts was bound up with the specific surface area as reported in prior studies [30,47].

From Figure 9d, it is obvious that the variation tendency of NH_3 conversion has a close resemblance to that of NO_2 conversion over Mn−Fe−Ce−O_x/γ-Al_2O_3 nanocatalysts. In the range of 25–200 °C, the NH_3 conversion was slightly higher than the NO_x conversion for each Mn−Fe−Ce−O_x/γ-Al_2O_3 nanocatalyst at the same temperature. Meanwhile, the NH_3 conversion reached above 99% for all tested catalysts within the temperature range of 200–350 °C. According to the results exhibited in Figure 9e, it can be basically confirmed that Mn−Fe−Ce−O_x/γ-Al_2O_3 nanocatalysts achieved satisfying N_2 selectivities. In the test temperature region, the Mn30−Ce/Al sample presented excellent N_2 selectivity that remained stable above 97.5%. The lowest N_2 selectivity was 88.3% obtained at 350 °C over the Mn15Fe15−Ce/Al sample. In order to better understand the enhancing effect of fast SCR on NO conversion than that of standard SCR, a contrast test was carried out under NO without NO_2 as shown in Figure 9f. Comparing the curves of Figure 9b,f, it could be confirmed that the participation of NO_2 in deNO_x reations boosted the NO conversion at relatively low temperature and broadened the active temperature window. Therefore, it was regarded as an effective method to improve NO_x conversion at low temperature by oxidizing NO to NO_2 and accelerating the fast SCR reaction.

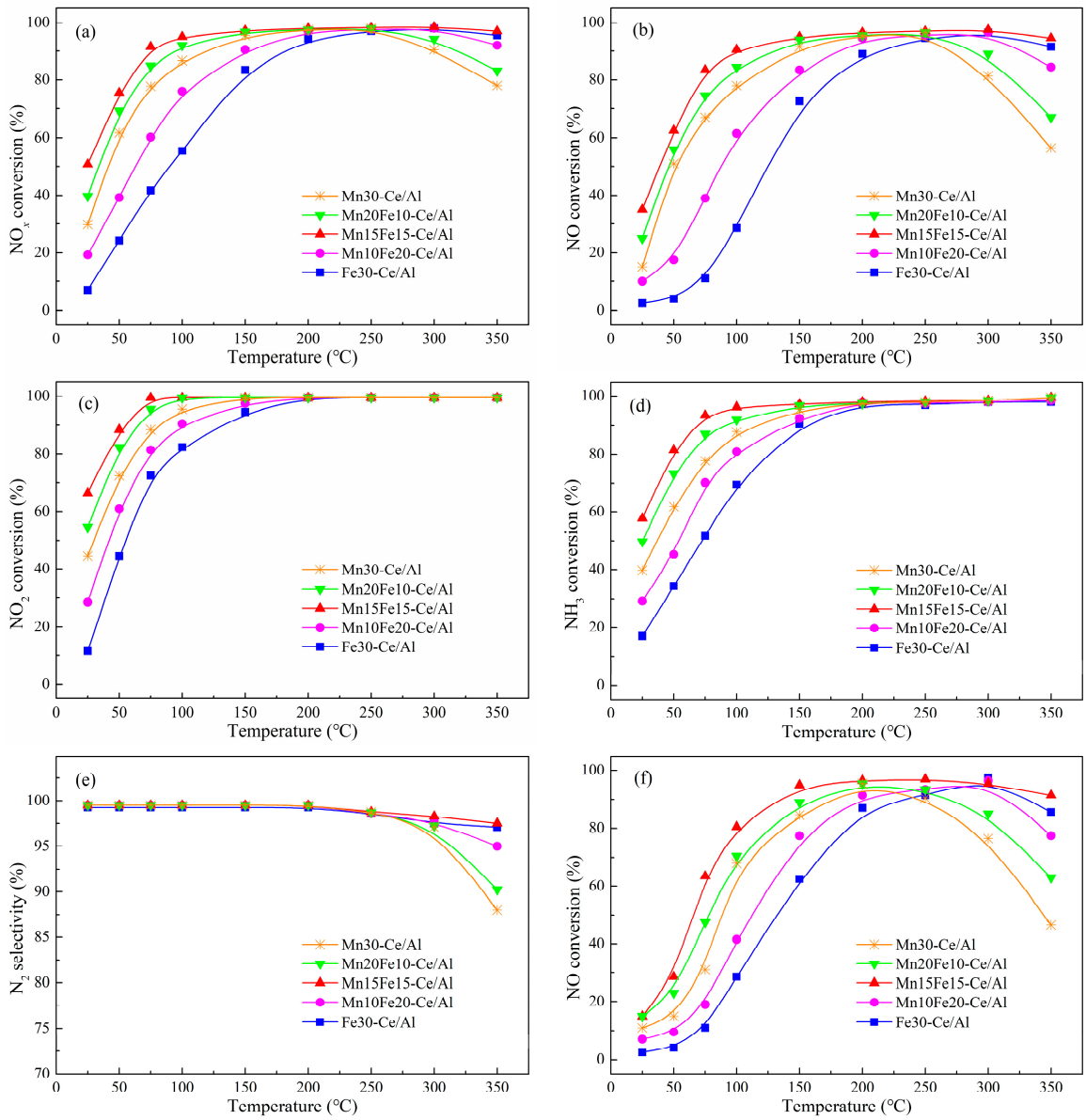

Figure 9. Fast SCR activity of Mn−Fe−Ce−O_x/γ-Al_2O_3 nanocatalysts. (**a**–**e**) 200 ppm NO, 200 ppm NO_2, 400 ppm NH_3, 5% O_2, ~0.3% H_2O and N_2 as balance gas; (**f**) 400 ppm NO, 400 ppm NH_3, 5% O_2, ~0.3% H_2O and N_2 as balance.

2.4. Reaction Mechanism Analysis

Based on the experiment data of physicochemical characteristics and catalytic performances of the tested catalyst samples exhibited above, the Mn/Fe molar ratio in Mn−Fe−Ce−O_x/γ-Al_2O_3 nanocatalysts influenced the oxidation and reduction characteristics of active chemisorbed sites notably, and changed the redox activities of active components significantly.

The synergistic effect among manganese, iron and cerium increased the percent of Mn^{4+}/Mn^{n+}, Fe^{3+}/Fe^{n+} and Ce^{3+}/Ce^{n+}, formed more lattice oxygen and plenty of oxygen vacancy on the catalyst surface [16]. Among the three tested catalyst samples in this study, the Mn15Fe15−Ce/Al sample with the Mn/Fe molar ratio of 1.0 presented the highest probability of nitrate intermediate formation via the oxidization of NO into NO_2, which was regarded as a pivotal catalytic step for accelerating the fast SCR reaction [47]. The fast SCR process mainly comprised four catalytic reactions [5]. Firstly, the disproportionation of NO_2 formed NO_2^- and NO_3^- on the catalyst [48,49]. Secondly, the formed NO_2^- reacted with NH_4^+ composing the intermediate NH_4NO_2 on the catalyst surface,

and then NH_4NO_2 decomposed rapidly into N_2 and H_2O. Thirdly, the formed NO_3^- reacted with NH_4^+ composing the intermediate NH_4NO_3 and further reacted with NO to produce NO_2, N_2 and H_2O. At the same time, some formed NO_3^- interacted with NO to produce NO_2^- and NO_2. Among these catalytic reactions, the NO transformation to NO_2 was considered as the crucial step in the reaction mechanism of fast SCR through the nitrate process. It had been revealed that MnO_2 was abundant in active oxygen and conducive to NO oxidation to NO_2 [37]. Mn^{4+} had the highest catalytic activity for NO elimination in consideration of the promotion effect on the reaction of NO oxidation to NO_2, which accelerated the fast SCR reaction remarkably [30]. Meanwhile, the MnO_2 phase presented better a catalytic property than Mn_2O_3 due to its lattice structure defect [50]. Therefore, Mn^{4+} achieved the strongest redox ability comparing to the other valence states in MnO_x-based catalysts [28]. The increase of the Mn^{4+}/Mn^{n+} ratio in the Mn15Fe15−Ce/Al sample indicated the species transformation from Mn^{3+} and Mn^{2+} to Mn^{4+}, and the chemical circumstance variation among the Mn10Fe20−Ce/Al, Mn15Fe15−Ce/Al and Mn20Fe10−Ce/Al samples. This variation was owing to the powerful interaction among manganese, iron and cerium with different Mn/Fe molar ratios, which had been fully proved by the results exhibited above. The increase of Mn^{4+} contained in the Mn15Fe15−Ce/Al sample was advantageous to NH_3 adsorption and beneficial to NO catalytic oxidation. The Mn^{4+}=O in the catalyst could react with NH_4^+ and NO to form Mn^{3+}−OH and release N_2 and H_2O. The formed Mn^{3+}−OH could interact with NO_3^- to turn back to Mn^{4+}=O and generate NO_2 and H_2O. As a result, the highest Mn^{4+}/Mn^{n+} ratio made a large contribution to intensify the fast SCR reaction [30]. Therefore, the Mn15Fe15−Ce/Al sample presented superior catalytic ability than the Mn10Fe20−Ce/Al and Mn20Fe10−Ce/Al samples.

Furthermore, it is proposed that the redox couples of Fe^{3+}/Fe^{2+} and Ce^{4+}/Ce^{3+} contained in Mn−Fe−Ce−O_x/γ-Al_2O_3 nanocatalysts strengthened the redox cycle of Mn^{4+}/Mn^{2+} and improve the amount of active oxygen, which would further promote the catalytic reactions [9,35]. The percentage of Fe^{2+}/Fe^{n+} and Ce^{3+}/Ce^{n+} improved with the Mn/Fe molar ratio of 1.0, probably attributed to the strong electron transfer between $Fe^{2+} \leftrightarrow Mn^{4+}$ [50], $Ce^{3+} \leftrightarrow Mn^{3+}$ [35] and $Ce^{3+} \leftrightarrow Mn^{4+}$ [37]. Hence, it is proposed that the appropriate Mn/Fe molar ratio could develop the intimate electronic interaction among manganese, iron and cerium. Comprehensive considering the XPS, H_2-TPR, NH_3-TPD and NO-TPD analysis in this study, the Mn−Fe−Ce−O_x/γ-Al_2O_3 nanocatalyst with the Mn/Fe molar ratio of 1.0 achieved the optimal physicochemical property in accordance with the catalytic performance. The possible redox catalytic pathway of fast SCR reaction over Mn−Fe−Ce−O_x/γ-Al_2O_3 nanocatalysts is exhibited in Figure 10.

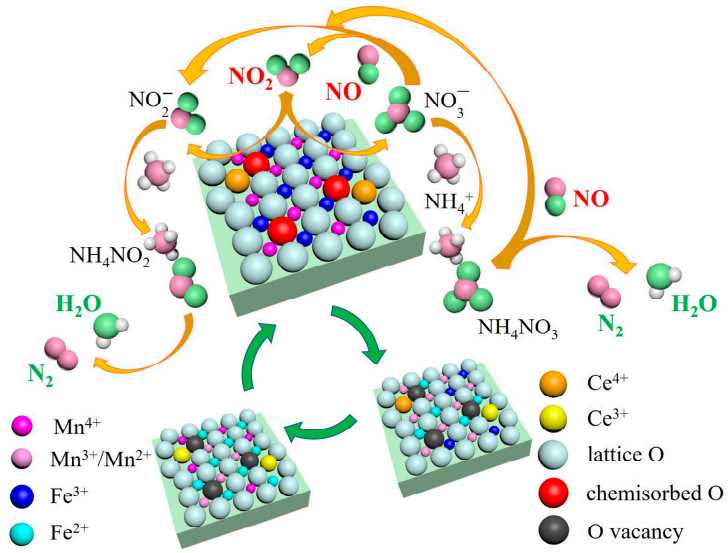

Figure 10. The possible redox catalytic pathway of the fast SCR reaction over Mn−Fe−Ce−O_x/γ-Al_2O_3 nanocatalysts.

3. Materials and Methods

3.1. Catalysts' Preparation

The Mn−Fe−Ce/Al nanocatalyst samples were prepared by the co-precipitation method. $Mn(NO_3)_2$ (analytical pure 50%, Sinopharm, Shanghai, China), $Fe(NO_3)_3 \cdot 9H_2O$ (analytical pure 99.9%, Sinopharm, Shanghai, China), and $Ce(NO_3)_3 \cdot 6H_2O$ (analytical pure 99.9%, Nanjing-reagent, Nanjing China) were introduced as the precursors of MnO_x, FeO_x and CeO_x, respectively. The nano γ-Al_2O_3 (ultra pure 99.99%, Aladdin, Seattle, Washington, USA) was used as the carrier for the active species. The precursors were all dissolved into deionized water followed by the addition of ammonia solution till pH rose to 8. Then, the nano γ-Al_2O_3 powder was put into the aqueous solution with continuous agitation to form a homogeneous gel. Subsequently, the gel was dried in N_2 at 150 °C for 24 h and calcinated at 450 °C for 4 h. Lastly, the generated Mn−Fe−Ce−O_x/γ-Al_2O_3 nanocatalysts were triturated and filtered with 40–60 mesh, at which sizes the diffusion effect on the catalytic performance was less than 0.5%. Hence, it could be regarded as no diffusional control with the catalytic activity calculations in this study. Meanwhile, the same size catalyst particles were used as the object for the characterization tests. In this contribution, a series of Mn−Fe−Ce−O_x/γ-Al_2O_3 samples with different Mn/Fe ratios were prepared and all samples were made up of (Mn+Fe) 30 wt% and Ce 5 wt%. The molar ratios of Mn:Fe were calculated on the basis of the mass ratios as displayed in Table 5.

Table 5. Contents of Ce, Fe and Mn on Mn−Fe−Ce−O_x/γ-Al_2O_3 nanocatalysts.

Samples	Mn		Fe		Ce		Mn:Fe
	Mass Fraction (%)	Molar Fraction (%)	Mass Fraction (%)	Molar Fraction (%)	Mass Fraction (%)	Molar Fraction (%)	MOLAR RATIO
Fe30−Ce/Al	0	0	30.0	93.8	5.0	6.2	–
Mn10Fe20−Ce/Al	10.0	31.3	20.0	62.5	5.0	6.2	0.5:1
Mn15Fe15−Ce/Al	15.0	47.0	15.0	46.8	5.0	6.2	1:1
Mn20Fe10−Ce/Al	20.0	62.6	10.0	31.2	5.0	6.2	2:1
Mn30−Ce/Al	30.0	93.9	0	0	5.0	6.1	–

3.2. Catalysts' Characterization

The Maxon Tristar II 3020 micropore-size analyzer (Micromeritics, Norcross, GA, USA) was introduced to test the N_2 adsorption isotherms of the nanocatalysts at −196 °C. The nanocatalysts were vacuum degassed at 350 °C for 10 h and then the surface areas and the pore-size distributions were measured. The specific surface areas were determined according to the BET plot linear portion. The pore-size distributions were calculated according to the desorption branch with the Barrett–Joyner–Halenda (BJH) formula. The XRD profiles were achieved by a Bruker D8 advance analyzer (Bruker, Billerica, MA, USA) with Mo K_α radiation. The diffraction intensity was tested from 10° to 90° with point counting time of 1s and step of 0.02°. International Center for Diffraction Data (ICDD) was used to distinguish the element phases in XRD patterns by comparing characteristic peaks. The surface image data on the nanocatalysts was captured by a FEI Quanta 400 FEG scanning electron microscope (FEI, Hillsboro, OR, USA), and the advanced microstructural and compositional information of the nanocatalysts was obtained by a high-resolution transmission electron microscope JEOL JEM-2010 (JEOL, Tokyo, Japan). The Micromeritics Autochem II 2920 chemical adsorption instrument (Micromeritics, Norcross, GA, USA) was employed to complete the H_2-TPR, NH_3-TPD and NO-TPD tests. In the H_2-TPR experiment, 50 mg nanocatalyst was pretreatment in He at 400 °C for 1 h, then was cooled to ambient temperature in the gas mixture of H_2 and He at 30 mL/min. The H_2 consumptions were tested within 50–850 °C at the heating rate of 10 °C/min. The experimental procedure of the NH_3-TPD and NO-TPD tests were quite similar to H_2-TPR test, with NH_3 and NO replacing H_2. XPS were analyzed via a Thermo ESCALAB 250XI under the pass energy of 46.95 eV, Al K_α radiation at 1486.6 eV, X-ray source at 150 W and binding energy precision within ± 0.3 eV. C 1*s* line at 284.6 eV was introduced as a reference.

3.3. Catalytic Performance Tests

The catalytic performance of Mn−Fe−Ce−O_x/γ-Al_2O_3 nanocatalysts for NO oxidation to NO_2 and fast SCR were explored in a fixed-bed reactor comprised of a tube furnace and a temperature control unit. All gas used in this experiment was controlled by mass flowmeters. The concentrations of NO and NO_2 were incessantly documented by a German MRU MGA-5 analyzer joint with an external special detector for N_2O and NH_3, as shown in Figure 11. During the experiment of NO oxidation into NO_2, the inlet gas contained 400 ppm NO, 5% O_2, ~0.3% H_2O and N_2 as balance gas. While in the test of fast SCR catalytic activity, the inlet mixed gas included 200 ppm NO, 200 ppm NO_2, 400 ppm NH_3, 5% O_2, ~0.3% H_2O and N_2 as balance gas. In the contrast experiment, 400 ppm NO was used instead of 200 ppm NO and 200 ppm NO_2. The whole flow rate was approximately 900 mL·min^{-1}, and the mass of the nanocatalyst for each run was 8.0 g. The gas hourly space velocity (GHSV) was about 25,000 h^{-1}. The NO oxidation rate and the NO_x conversion rate were calculated by the concentrations of NO_x, NO and NO_2 according to Equations (5) and (6), where $[NO_x] = [NO] + [NO_2]$. The NH_3 conversion rate was calculated by the inlet and outlet NH_3 concentrations, and the N_2 selectivity was calculated by the concentrations of N_2O and NO_x, as show in Equations (7) and (8) [51–53]. Each experiment was repeated three times to assure the results' accuracy.

$$\text{NO oxidation rate} = \frac{[\text{NO}]_{\text{in}} - [\text{NO}]_{\text{out}}}{[\text{NO}]_{\text{in}}} \times 100\% \tag{5}$$

$$\text{NO}_x \text{ conversion rate} = \frac{[\text{NO}_x]_{\text{in}} - [\text{NO}_x]_{\text{out}}}{[\text{NO}_x]_{\text{in}}} \times 100\% \tag{6}$$

$$\text{NH}_3 \text{ conversion rate} = \frac{[\text{NH}_3]_{\text{in}} - [\text{NH}_3]_{\text{out}}}{[\text{NH}_3]_{\text{in}}} \times 100\% \tag{7}$$

$$\text{N}_2 \text{ selectivity} = 1 - \frac{2[\text{N}_2\text{O}]_{\text{out}}}{[\text{NO}_x]_{\text{in}} - [\text{NO}_x]_{\text{out}}} \times 100\% \tag{8}$$

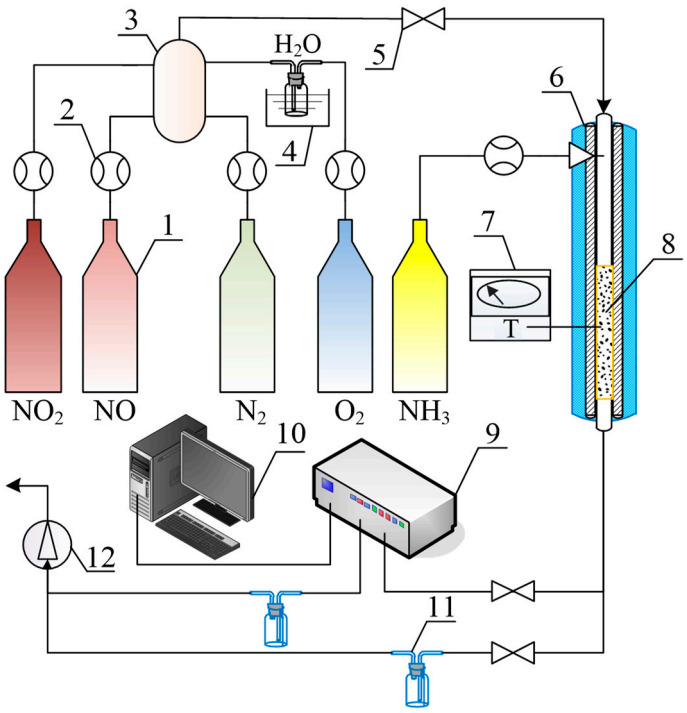

Figure 11. The schematic diagrams of the catalytic performance tests. 1, standard gas; 2, mass flowmeter; 3, gas mixer; 4, water carrier; 5, shutdown valve; 6, resistance furnace; 7, temperature controller; 8, catalysts; 9, flue gas analyzer; 10, record system; 11, gas washing bottle; 12, induced draft fan.

4. Conclusions

Mn−Fe−Ce−O_x/γ-Al_2O_3 nanocatalysts with different Mn/Fe ratios were synthesized to research the catalytic oxidation of NO into NO_2 and the catalytic performance in the fast SCR reaction, in order to explore the strong interactions among manganese, iron and cerium. According to the physicochemical properties of the Mn10Fe20−Ce/Al, Mn15Fe15−Ce/Al and Mn20Fe10−Ce/Al nanocatalysts, it could be concluded that the Mn15Fe15−Ce/Al sample with Mn/Fe molar ratio of 1.0 achieved the optimal coexistence of manganese, iron and cerium, enhanced the active species distribution, and restrained the metal oxide crystallinity. In the meantime, it was found that the ratios of Mn^{4+}/Mn^{n+}, Fe^{2+}/Fe^{n+} and Ce^{3+}/Ce^{n+} presented the maximum in Mn15Fe15−Ce/Al sample, which were beneficial to enrich oxygen vacancy and chemisorbed oxygen on the catalyst, and were conducive to facilitate the fast SCR process by promoting the possibility of NO catalytic oxidation into NO_2. The performance of NO oxidation and fast SCR catalytic activity over Mn−Fe−Ce−O_x/γ-Al_2O_3 nanocatalysts were in accordance with the structural results. Among all the tested samples, the Mn15Fe15−Ce/Al sample presented the highest catalytic ability in the oxidation of NO into NO_2 (64.2%, 350 °C) and the optimal NO_x conversion of fast SCR (>90%, 75~350 °C). Overall, it was believed that the optimization of the Mn/Fe ratio in Mn−Fe−Ce−O_x/γ-Al_2O_3 nanocatalysts was an extremely effective method to improve the structure–activity relationships for NO pre-oxidation and the fast SCR reaction.

Author Contributions: Conceptualization, Y.G.; Funding acquisition, Y.G., T.L., W.Z.; Methodology, Y.G., T.L.; Project administration, Y.G.; Writing—original draft, Y.G.; Writing—review and editing, M.Z. and W.Z.; Data curation, Y.G., W.F.

Funding: This research was funded by "National Natural Science Foundation of China, grant number 51708336", "Shandong Provincial Natural Science Foundation, grant number ZR2016EEB28", "Shandong Provincial Science and Technology Development Plan, grant number 2011GSF11716", "Shandong Jianzhu University Doctoral Research Fund, grant number X18069Z", "Shandong Jianzhu University Open Experimental Project, grant number 2018yzkf023, 2018wzkf013", and "Shandong Electric Power Engineering Consulting Institute Science and Technology Project, grant number 37-K2014-33".

Acknowledgments: This work was supported by National Natural Science Foundation of China (Project No.51708336), Shandong Provincial Natural Science Foundation (ZR2016EEB28), Shandong Provincial Science and Technology Development Plan (2011GSF11716), Shandong Jianzhu University open experimental project (2018yzkf023, 2018wzkf013), and the Shandong electric power engineering consulting institute science and technology project (37-K2014-33).

Conflicts of Interest: The authors declare no conflict of interest.

References

1. Zhou, H.; Ge, M.Y.; Wu, S.G.; Ye, B.C.; Su, Y.X. Iron based monolithic catalysts supported on Al_2O_3, SiO_2, and TiO_2: A comparison for NO reduction with propane. *Fuel* **2018**, *220*, 330–338. [CrossRef]
2. Roy, S.; Hegde, M.S.; Madras, G. Catalysis for NO_x abatement. *Appl. Energy* **2009**, *86*, 2283–2297. [CrossRef]
3. Zhou, X.; Huang, X.; Xie, A.; Luo, S.; Yao, C.; Li, X.; Zuo, S. V_2O_5-decorated Mn-Fe/attapulgite catalyst with high SO_2 tolerance for SCR of NO_x with NH_3 at low temperature. *Chem. Eng. J.* **2017**, *326*, 1074–1085. [CrossRef]
4. Bendrich, M.; Scheuer, A.; Hayes, R.E.; Votsmeier, M. Unified mechanistic model for Standard SCR, Fast SCR, and NO_2 SCR over a copper chabazite catalyst. *Appl. Catal. B Environ.* **2018**, *222*, 76–87. [CrossRef]
5. Ruggeri, M.P.; Grossale, A.; Nova, I.; Tronconi, E.; Jirglova, H.; Sobalik, Z. FTIR in situ mechanistic study of the NH_3NO/NO_2 "Fast SCR" reaction over a commercial Fe-ZSM-5 catalyst. *Catal. Today* **2012**, *184*, 107–114. [CrossRef]
6. Koebel, M.; Elsener, M. Selective catalytic reduction of NO over commercial $DeNO_x$-catalysts: Experimental determination of kinetic and thermodynamic parameters. *Chem. Eng. Sci.* **1998**, *53*, 657–669. [CrossRef]
7. Gao, Y.; Luan, T.; Lu, T.; Cheng, K.; Xu, H. Performance of V_2O_5-WO_3-MoO $_3/TiO_2$ catalyst for selective catalytic reduction of NO_x by NH_3. *Chin. J. Chem. Eng.* **2013**, *21*, 1–7. [CrossRef]
8. Li, G.; Wang, B.; Wang, H.; Ma, J.; Xu, W.Q.; Li, Y.; Han, Y.; Sun, Q. Fe and/or Mn oxides supported on fly ash-derived SBA-15 for low-temperature NH_3-SCR. *Catal. Commun.* **2018**, *108*, 82–87. [CrossRef]

9. Zhang, C.; Chen, T.; Liu, H.; Chen, D.; Xu, B.; Qing, C. Low temperature SCR reaction over Nano-Structured Fe-Mn Oxides: Characterization, performance, and kinetic study. *Appl. Surf. Sci.* **2018**, *457*, 1116–1125. [CrossRef]
10. Huang, T.-J.; Zhang, Y.-P.; Zhuang, K.; Lu, B.; Zhu, Y.-W.; Shen, K. Preparation of honeycombed holmium-modified Fe-Mn/TiO_2 catalyst and its performance in the low temperature selective catalytic reduction of NO_x. *J. Fuel Chem. Technol.* **2018**, *46*, 319–327. [CrossRef]
11. Ke, Z.; Feng, Y.; Mingyuan, Z.; Jianming, D.; Xugen, W.; Jinli, Z.; Bin, D. Enhanced Low Temperature NO Reduction Performance via MnO_x-Fe_2O_3/Vermiculite Monolithic Honeycomb Catalysts. *Catalysts* **2018**, *8*, 100. [CrossRef]
12. Wang, X.; Wu, S.; Zou, W.; Yu, S.; Gui, K.; Dong, L. Fe-Mn/Al_2O_3 catalysts for low temperature selective catalytic reduction of NO with NH_3. *Chin. J. Catal.* **2016**, *37*, 1314–1323. [CrossRef]
13. Zhang, M.; Li, C.; Qu, L.; Fu, M.; Zeng, G.; Fan, C.; Ma, J.; Zhan, F. Catalytic oxidation of NO with O_2 over $FeMnO_x$/TiO_2: Effect of iron and manganese oxides loading sequences and the catalytic mechanism study. *Appl. Surf. Sci.* **2014**, *300*, 58–65. [CrossRef]
14. Fang, N.; Guo, J.; Shu, S.; Luo, H.; Chu, Y.; Li, J. Enhancement of low-temperature activity and sulfur resistance of $Fe_{0.3}Mn_{0.5}Zr_{0.2}$ catalyst for NO removal by NH_3-SCR. *Chem. Eng. J.* **2017**, *325*, 114–123. [CrossRef]
15. Boningari, T.; Pappas, D.K.; Ettireddy, P.R.; Kotrba, A.; Smirniotis, P.G. Influence of SiO_2 on M/TiO_2 (M = Cu, Mn, and Ce) Formulations for Low-Temperature Selective Catalytic Reduction of NO_x with NH_3: Surface Properties and Key Components in Relation to the Activity of NO_x Reduction. *Ind. Eng. Chem. Res.* **2015**, *54*, 2261–2273. [CrossRef]
16. France, L.J.; Yang, Q.; Li, W.; Chen, Z.; Guang, J.; Guo, D.; Wang, L.; Li, X. Ceria modified $FeMnO_x$—Enhanced performance and sulphur resistance for low-temperature SCR of NO_x. *Appl. Catal. B Environ.* **2017**, *206*, 203–215. [CrossRef]
17. Cao, L.; Chen, L.; Wu, X.; Ran, R.; Xu, T.; Chen, Z.; Weng, D. TRA and DRIFTS studies of the fast SCR reaction over CeO_2/TiO_2 catalyst at low temperatures. *Appl. Catal. A Gen.* **2018**, *557*, 46–54. [CrossRef]
18. Panahi, P.N.; Delahay, G.; Mousavi, S.M. Activity of gamma-Al_2O_3-based Mn, Cu, and Co oxide nanocatalysts for selective catalytic reduction of nitric oxide with ammonia. *Turk. J. Chem.* **2017**, *41*, 272–281. [CrossRef]
19. Zhao, W.; Tang, Y.; Wan, Y.; Li, L.; Yao, S.; Li, X.; Gu, J.; Li, Y.; Shi, J. Promotion effects of SiO_2 or/and Al_2O_3 doped CeO_2/TiO_2 catalysts for selective catalytic reduction of NO by NH_3. *J. Hazard. Mater.* **2014**, *278*, 350–359. [CrossRef]
20. Xu, H.; Liu, S.; Wang, Y.; Lin, Q.; Lin, C.; Lan, L.; Wang, Q.; Chen, Y. Promotional effect of Al_2O_3 on WO_3/CeO_2-ZrO_2 monolithic catalyst for selective catalytic reduction of nitrogen oxides with ammonia after hydrothermal aging treatment. *Appl. Surf. Sci.* **2018**, *427*, 656–669. [CrossRef]
21. Gao, Y.; Luan, T.; Zhang, W.; Li, H. The promotional effects of cerium on the catalytic properties of Al_2O_3-supported $MnFeO_x$ for NO oxidation and fast SCR reaction. *Res. Chem. Intermed.* **2018**, in press. [CrossRef]
22. Wang, C.; Yu, F.; Zhu, M.; Wang, X.; Dan, J.; Zhang, J.; Cao, P.; Dai, B. Microspherical MnO_2-CeO_2-Al_2O_3 mixed oxide for monolithic honeycomb catalyst and application in selective catalytic reduction of NO_x with NH_3 at 50–150 °C. *Chem. Eng. J.* **2018**, *346*, 182–192. [CrossRef]
23. Qin, C.; Dang, X.; Huang, J.; Teng, J.; Huang, X. Plasma-catalytic oxidation of adsorbed toluene on Ag–Mn/γ-Al_2O_3: Comparison of gas flow-through and gas circulation treatment. *Chem. Eng. J.* **2016**, *299*, 85–92. [CrossRef]
24. Fu, H.; Sun, S.; Yang, X.; Li, W.; An, X.; Zhang, H.; Dong, Y.; Jiang, X.; Yu, A. A facile coating method to construct uniform porous α-Fe_2O_3@TiO_2 core-shell nanostructures with enhanced solar light photocatalytic activity. *Powder Technol.* **2018**, *328*, 389–396. [CrossRef]
25. Kapteijn, F.; Singoredjo, L.; Andreini, A.; Moulijn, J.A. Activity and selectivity of pure manganese oxides in the selective catalytic reduction of nitric oxide with ammonia. *Appl. Catal. B Environ.* **1994**, *3*, 173–189. [CrossRef]
26. Pérez Vélez, R.; Ellmers, I.; Huang, H.; Bentrup, U.; Schünemann, V.; Grünert, W.; Brückner, A. Identifying active sites for fast NH_3-SCR of NO/NO_2 mixtures over Fe-ZSM-5 by operando EPR and UV–vis spectroscopy. *J. Catal.* **2014**, *316*, 103–111. [CrossRef]

27. Schwidder, M.; Heikens, S.; De Toni, A.; Geisler, S.; Berndt, M.; Brückner, A.; Grünert, W. The role of NO_2 in the selective catalytic reduction of nitrogen oxides over Fe-ZSM-5 catalysts: Active sites for the conversion of NO and of NO/NO_2 mixtures. *J. Catal.* **2008**, *259*, 96–103. [CrossRef]
28. Wang, C.; Yu, F.; Zhu, M.; Tang, C.; Dong, L.; Dai, B. Synthesis of Both Powdered and Preformed MnO_x-CeO_2-Al_2O_3 Catalysts by Self-Propagating High-Temperature Synthesis for the Selective Catalytic Reduction of NO_x with NH_3. *ACS Omega* **2018**, *3*, 5692–5703. [CrossRef]
29. Gao, G.; Shi, J.-W.; Liu, C.; Gao, C.; Fan, Z.; Niu, C. Mn/CeO_2 catalysts for SCR of NO_x with NH_3: Comparative study on the effect of supports on low-temperature catalytic activity. *Appl. Surf. Sci.* **2017**, *411*, 338–346. [CrossRef]
30. Wang, T.; Wan, Z.; Yang, X.; Zhang, X.; Niu, X.; Sun, B. Promotional effect of iron modification on the catalytic properties of Mn-Fe/ZSM-5 catalysts in the Fast SCR reaction. *Fuel Process. Technol.* **2018**, *169*, 112–121. [CrossRef]
31. Huang, B.; Yu, D.; Sheng, Z.; Yang, L. Novel CeO_2@TiO_2 core–shell nanostructure catalyst for selective catalytic reduction of NO_x with NH_3. *J. Environ. Sci.* **2017**, *55*, 129–136. [CrossRef] [PubMed]
32. Boningari, T.; Somogyvari, A.; Smirniotis, P.G. Ce-Based Catalysts for the Selective Catalytic Reduction of NO_x in the Presence of Excess Oxygen and Simulated Diesel Engine Exhaust Conditions. *Ind. Eng. Chem. Res.* **2017**, *56*, 5483–5494. [CrossRef]
33. Yao, X.; Zhao, R.; Chen, L.; Du, J.; Tao, C.; Yang, F.; Dong, L. Selective catalytic reduction of NO_x by NH_3 over CeO_2 supported on TiO_2: Comparison of anatase, brookite, and rutile. *Appl. Catal. B Environ.* **2017**, *208*, 82–93. [CrossRef]
34. Yang, S.; Liao, Y.; Xiong, S.; Qi, F.; Dang, H.; Xiao, X.; Li, J. N_2 Selectivity of NO Reduction by NH_3 over MnO_x-CeO_2: Mechanism and Key Factors. *J. Phys. Chem. C* **2014**, *118*, 21500–21508. [CrossRef]
35. Wang, B.; Chi, C.; Xu, M.; Wang, C.; Meng, D. Plasma-catalytic removal of toluene over CeO_2-MnO_x catalysts in an atmosphere dielectric barrier discharge. *Chem. Eng. J.* **2017**, *322*, 679–692. [CrossRef]
36. Xiong, Y.; Tang, C.; Yao, X.; Zhang, L.; Li, L.; Wang, X.; Deng, Y.; Gao, F.; Dong, L. Effect of metal ions doping (M = Ti^{4+}, Sn^{4+}) on the catalytic performance of MnO_x/CeO_2 catalyst for low temperature selective catalytic reduction of NO with NH_3. *Appl. Catal. A Gen.* **2015**, *495*, 206–216. [CrossRef]
37. Yao, X.; Ma, K.; Zou, W.; He, S.; An, J.; Yang, F.; Dong, L. Influence of preparation methods on the physicochemical properties and catalytic performance of MnO_x-CeO_2 catalysts for NH_3-SCR at low temperature. *Chin. J. Catal.* **2017**, *38*, 146–159. [CrossRef]
38. Zhu, X.; Tu, X.; Mei, D.; Zheng, C.; Zhou, J.; Gao, X.; Luo, Z.; Ni, M.; Cen, K. Investigation of hybrid plasma-catalytic removal of acetone over CuO/γ-Al_2O_3 catalysts using response surface method. *Chemosphere* **2016**, *155*, 9–17. [CrossRef]
39. Stanciulescu, M.; Caravaggio, G.; Dobri, A.; Moir, J.; Burich, R.; Charland, J.P.; Bulsink, P. Low-temperature selective catalytic reduction of NO_x with NH_3 over Mn-containing catalysts. *Appl. Catal. B Environ.* **2012**, *123–124*, 229–240. [CrossRef]
40. Chen, Z.; Wang, F.; Li, H.; Yang, Q.; Wang, L.; Li, X. Low-Temperature Selective Catalytic Reduction of NO_x with NH_3 over Fe–Mn Mixed-Oxide Catalysts Containing $Fe_3Mn_3O_8$ Phase. *Ind. Eng. Chem. Res.* **2012**, *51*, 202–212. [CrossRef]
41. Cao, F.; Su, S.; Xiang, J.; Wang, P.; Hu, S.; Sun, L.; Zhang, A. The activity and mechanism study of Fe–Mn–Ce/γ-Al_2O_3 catalyst for low temperature selective catalytic reduction of NO with NH_3. *Fuel* **2015**, *139*, 232–239. [CrossRef]
42. Wu, S.; Yao, X.; Zhang, L.; Cao, Y.; Zou, W.; Li, L.; Ma, K.; Tang, C.; Gao, F.; Dong, L. Improved low temperature NH_3-SCR performance of $FeMnTiO_x$ mixed oxide with CTAB-assisted synthesis. *Chem. Commun.* **2015**, *51*, 3470–3473. [CrossRef] [PubMed]
43. Cheng, X.; Zhang, X.; Su, D.; Wang, Z.; Chang, J.; Ma, C. NO reduction by CO over copper catalyst supported on mixed CeO_2 and Fe_2O_3: Catalyst design and activity test. *Appl. Catal. B Environ.* **2018**, *239*, 485–501. [CrossRef]
44. Jin, R.; Liu, Y.; Wu, Z.; Wang, H.; Gu, T. Low-temperature selective catalytic reduction of NO with NH_3 over MnCe oxides supported on TiO_2 and Al_2O_3: A comparative study. *Chemosphere* **2010**, *78*, 1160–1166. [CrossRef] [PubMed]
45. Grossale, A.; Nova, I.; Tronconi, E. Ammonia blocking of the "Fast SCR" reactivity over a commercial Fe-zeolite catalyst for Diesel exhaust aftertreatment. *J. Catal.* **2009**, *265*, 141–147. [CrossRef]

46. Nova, I.; Ciardelli, C.; Tronconi, E.; Chatterjee, D.; Bandl-Konrad, B. NH_3-SCR of NO over a V-based catalyst: Low-T redox kinetics with NH_3 inhibition. *AIChE J.* **2006**, *52*, 3222–3233. [CrossRef]
47. Gao, C.; Shi, J.-W.; Fan, Z.; Wang, B.; Wang, Y.; He, C.; Wang, X.; Li, J.; Niu, C. "Fast SCR" reaction over Sm-modified MnO_x-TiO_2 for promoting reduction of NO_x with NH_3. *Appl. Catal. A Gen.* **2018**, *564*, 102–112. [CrossRef]
48. Grossale, A.; Nova, I.; Tronconi, E.; Chatterjee, D.; Weibel, M. The chemistry of the NO/NO_2–NH_3 "fast" SCR reaction over Fe-ZSM_5 investigated by transient reaction analysis. *J. Catal.* **2008**, *256*, 312–322. [CrossRef]
49. Iwasaki, M.; Shinjoh, H. A comparative study of "standard", "fast" and "NO_2" SCR reactions over Fe/zeolite catalyst. *Appl. Catal. A Gen.* **2010**, *390*, 71–77. [CrossRef]
50. Li, Y.; Li, Y.; Wang, P.; Hu, W.; Zhang, S.; Shi, Q.; Zhan, S. Low-temperature selective catalytic reduction of NO_x with NH_3 over $MnFeO_x$ nanorods. *Chem. Eng. J.* **2017**, *330*, 213–222. [CrossRef]
51. Chen, L.; Li, J.; Ablikim, W.; Wang, J.; Chang, H.; Ma, L.; Xu, J.; Ge, M.; Arandiyan, H. CeO_2–WO_3 Mixed Oxides for the Selective Catalytic Reduction of NO_x by NH_3 Over a Wide Temperature Range. *Catal. Lett.* **2011**, *141*, 1859–1864. [CrossRef]
52. Liu, Z.; Yi, Y.; Zhang, S.; Zhu, T.; Zhu, J.; Wang, J. Selective catalytic reduction of NO_x with NH_3 over Mn-Ce mixed oxide catalyst at low temperatures. *Catal. Today* **2013**, *216*, 76–81. [CrossRef]
53. Yang, S.; Li, J.; Wang, C.; Chen, J.; Ma, L.; Chang, H.; Chen, L.; Peng, Y.; Yan, N. Fe-Ti spinel for the selective catalytic reduction of NO with NH_3: Mechanism and structure-activity relationship. *Appl. Catal. B Environ.* **2012**, *117–118*, 73–80. [CrossRef]